CIRCULAR SENSOR ARRAY AND NONLINEAR

ANALYSIS OF HOMOPOLAR MAGNETIC BEARINGS

A Thesis

by

ROBERT KYLE WIESENBORN

Submitted to the Office of Graduate Studies of
Texas A&M University
in partial fulfillment of the requirements for the degree of

MASTER OF SCIENCE

December 2006

Major Subject: Mechanical Engineering

CIRCULAR SENSOR ARRAY AND NONLINEAR

ANALYSIS OF HOMOPOLAR MAGNETIC BEARINGS

A Thesis

by

ROBERT KYLE WIESENBORN

Submitted to the Office of Graduate Studies of
Texas A&M University
in partial fulfillment of the requirements for the degree of

MASTER OF SCIENCE

Approved by:

Chair of Committee,	Alan B. Palazzolo
Committee Members,	John M. Vance
	Thomas W. Strganac
Head of Department,	Dennis L. O'Neal

December 2006

Major Subject: Mechanical Engineering

ABSTRACT

Circular Sensor Array and Nonlinear Analysis
of Homopolar Magnetic Bearings. (December 2006)
Robert Kyle Wiesenborn, B.S., Texas A&M University
Chair of Advisory Committee: Dr. Alan B. Palazzolo

Magnetic bearings use variable attractive forces generated by electromagnetic control coils to support rotating shafts with low friction and no material wear while providing variable stiffness and damping. Rotor deflections are stabilized by position feedback control along two axes using non-contacting displacement sensors. These sensor signals contain sensor runout error which can be represented by a Fourier series composed of harmonics of the spin frequency. While many methods have been proposed to compensate for these runout harmonics, most are computationally intensive and can destabilize the feedback loop. One attractive alternative is to increase the number of displacement sensors and map individual probe voltages to the two independent control signals. This approach is implemented using a circular sensor array and single weighting gain matrix in the present work. Analysis and simulations show that this method eliminates runout harmonics from 2 to n-2 when all sensors in an ideal n-sensor array are operational. Sensor failures result in reduced synchronous amplitude and increased harmonic amplitudes after failure. These amplitudes are predicted using derived expressions and synchronous measurement error can be corrected using an adjustment factor for single failures. A prototype 8-sensor array shows substantial runout reduction and bandwidth and sensitivity comparable to commercial systems.

Nonlinear behavior in homopolar magnetic bearings is caused primarily by the quadratic relationship between coil currents and magnetic support forces. Governing equations for a permanent magnet biased homopolar magnetic bearing are derived using magnetic circuit equations and linearized using voltage and position stiffness terms. Nonlinear hardening and softening spring behavior is achieved by varying proportional

control gain and frequency response is determined for one case using numerical integration and a shooting algorithm. Maximum amplitudes and phase reversal for this nonlinear system occur at lower frequencies than the linearized system. Rotor oscillations exhibit amplitude jumps by cyclic fold bifurcations, creating a region of hysteresis where multiple stable equilibrium states exist. One of these equilibrium states contains subharmonic frequency components resulting in quasiperiodic rotor motion. This nonlinear analysis shows how nonlinear rotor oscillations can be avoided for a wide range of operation by careful selection of design parameters and operating conditions.

ACKNOWLEDGMENTS

I would like to express my appreciation to Dr. Palazzolo for his guidance and patience in helping me complete this research, for the experience gained while working in the Vibration Control and Electromagnetics Laboratory and for the knowledge and understanding of vibrations and control systems learned in his courses. I would also like to thank Erwin Thomas for designing and building the sensor array drive circuit and for helping me understand how it works and to Dr. John Vance and Dr. Tom Strganac for serving on my advisory committee.

This work would not have been possible without the encouragement and support of my loving wife Lindsey, to whom I dedicate this research.

TABLE OF CONTENTS

		Page
ABSTRACT……		iii
ACKNOWLEDGMENTS……..…….....		v
TABLE OF CONTENTS……		vi
LIST OF FIGURES…….		viii
LIST OF TABLES…….....		x
CHAPTER		
I	INTRODUCTION……..……...	1
	1.1 Overview……..……...	1
	1.2 Literature Review…….....	3
	1.3 Research Objectives…….….....	6
	1.4 Organization…….....	7
	1.5 Original Contributions……...	8
II	CIRCULAR SENSOR ARRAY…….	9
	2.1 Introduction……..	9
	2.2 Description of Sensor Array……	11
	2.3 Numerical Simulation and Results……..	15
	Single Sensor Failures……	22
	Double Sensor Failures……..	28
	2.4 Design of Sensor Array Prototype……..	32
	2.5 Testing of Sensor Array Prototype…….	36
	2.6 Testing Results……	40
	2.7 Summary and Future Work……	50
III	NONLINEAR ANALYSIS OF HOMOPOLAR MAGNETIC BEARINGS…….	51
	3.1 Introduction…….	51
	3.2 System Model…….	53
	Nonlinear Model……	55
	Linear Model…….	63
	3.3 Frequency Response……..……	67
	3.4 Shooting Method…….……..	74

CHAPTER Page

3.5 Bifurcation Analysis……. 78
3.6 Summary…… 88

IV CONCLUSIONS……..…… 89

4.1 Circular Sensor Array……..…….. 89
4.2 Nonlinear Analysis of
Homopolar Magnetic Bearings……. 91
4.3 Future Work……...…… 93

REFERENCES…….. 95

APPENDIX A……... 97

VITA……. 98

LIST OF FIGURES

FIGURE		Page
2.1	Circular 8-sensor array …….	11
2.2	Runout signal used for numerical simulation in time and frequency domains……..	16
2.3	Attenuation of runout harmonics using 8-sensor array, no failures……..	18
2.4	DC shift using 8-sensor array, sensor 1 failed, non-zero bias……...	20
2.5	Attenuation of runout harmonics using 16-sensor array, no failures……..…….	24
2.6	Positioning fixture used for stationary gap measurements……	37
2.7	Rotating test fixture used for runout evaluation……	38
2.8	Runout signal used to evaluate reduction of harmonic amplitudes……...	39
2.9	Fourier amplitudes of modified runout signal……	39
2.10	Sensor array voltage vs position for x1-axis……..	41
2.11	Sensor array voltage vs position for x2-axis……..	41
2.12	Broadband noise amplitude for 8-sensor array and Bently Nevada *Proximitor*……..	43
2.13	Frequency spectrum of vibration and runout measured by a single sensor……..	45
2.14	Frequency spectrum of test rotor runout measured by 8-sensor array……	47
2.15	Peak-hold frequency spectrum of commercial sensor and 8-sensor array prototype……..	48
3.1	Rigid rotor-bearing model used for analysis…….	54
3.2	Magnetic circuit used to solve for coil currents and magnetic field strength…….	56
3.3	Permanent magnet demagnetization curve……	58
3.4	Control strategy used in the homopolar magnetic bearing……	61
3.5	Nonlinear magnetic force vs rotor position for linearized position stiffness…….	64

FIGURE Page

3.6 Nonlinear magnetic force vs control voltage for linearized voltage stiffness…….. 65

3.7 Effect of proportional control gain on magnetic bearing stiffness……... 69

3.8 X-axis amplitude frequency response for softening spring behavior……... 71

3.9 X-axis phase frequency response for softening spring behavior…….. 73

3.10 X-amplitude frequency response for stable and unstable equilibrium states……. 77

3.11 Migration of Floquet multiplier near upward amplitude jump bifurcation……... 79

3.12 Bifurcation diagram for decreasing speed……. 81

3.13 Bifurcation diagram for decreasing speeds near nonlinear resonance…….. 82

3.14 Bifurcation diagram for decreasing speeds near ω=394 $^{rad}/_{s}$ ……. 83

3.15 Poincaré map at ω=393 $^{rad}/_{s}$ showing quasiperiodic response…….. 84

3.16 Frequency spectrum for quasiperiodic response at 392 $^{rad}/_{s}$ …….. 85

3.17 X-position time signal for quasiperiodic oscillations…… 86

3.18 Rotor orbit for stable period-two equilibrium state at 387 $^{rad}/_{s}$ …….. 87

LIST OF TABLES

TABLE		Page
2.1	Harmonic amplitudes for 8-sensor array, sensor 1 failed…….	22
2.2	Harmonic amplitudes for 8-sensor array, sensor 2 failed…….	23
2.3	Harmonic amplitudes for 16-sensor array, sensor 1 failed…….	25
2.4	Harmonic amplitudes for 16-sensor array, sensor 2 failed…….	26
2.5	Harmonic amplitudes for 8-sensor array, sensor 2 failed, amplitude adjusted…….	28
2.6	Harmonic amplitudes for 8-sensor array, sensors 1 & 5 failed…….	29
2.7	Harmonic amplitudes for 8-sensor array, sensors 2 & 6 failed…….	30
2.8	Harmonic amplitudes for 16-sensor array, sensors 2 & 10 failed……...	31
2.9	Noise amplitudes for sensor array prototype and commercial system……...	44
2.10	Harmonic amplitudes measured using a single sensor and 8-sensor array with runout and measurement error…….	46
3.1	Mass properties of model rotor-bearing system……..	54
3.2	Properties of magnetic bearing poles and permanent magnets used in analysis……	60
3.3	Control gains used to analyze softening spring behavior……...…	70
3.4	Shooting algorithm parameters and values…….	75

CHAPTER I

INTRODUCTION

1.1 OVERVIEW

Active magnetic bearings (AMBs) provide an opportunity to address many classical rotordynamics problems in novel ways not possible with conventional roller or fluid film bearings. Frictionless, wear-free operation and the ability to vary stiffness and damping coefficients for different operating conditions make magnetic bearings attractive alternatives for many challenging applications. Magnetic bearings have been utilized in turbomachinery such as turbines and compressors, aircraft engines, flywheel energy storage systems and even for attitude control of satellites. Application in such sensitive rotordynamic systems necessitates extensive research into AMB control systems and nonlinear behavior to reliably levitate spinning rotors and control unbalance vibrations.

Magnetic bearings use forces generated by coil-wound electromagnets to support static rotor weight and control dynamic rotor oscillations due to mass unbalance. Magnetic forces are actively varied using currents determined by position feedback control. Due to the quadratic nature of these magnetic forces, magnetic bearings are inherently nonlinear systems. These nonlinearities result in bifurcation behavior as system parameters are varied, sensitivity to initial conditions, and steady state response with subharmonic frequency components. There are two types of magnetic bearings which are classified by the flux path of electromagnetic poles. In heteropolar magnetic bearings pole pairs are arranged circumferentially around the rotor so that flux paths are primarily radial in nature. In homopolar magnetic bearings pole pairs are aligned axially along the shaft so that flux paths have both radial and axial components. For the homopolar configuration magnetic polarities of circumferential tracks around the rotor do not change during rotation, reducing parasitic drag effects. While extensive research

---

This thesis follows the style and format of *Journal of Sound and Vibration*.

has been performed on the nonlinear characteristics of heteropolar magnetic bearings, nonlinearities in homopolar magnetic bearings have not yet been fully studied.

Behavior of active magnetic bearings is strongly influenced by the sensor feedback signal used by the controller to determine control currents. Magnetic bearings are particularly susceptible to sensor disturbance due to high speed applications requiring extreme precision. In AMB control systems, an accurate measurement of the shaft centerline displacement is vital to maintain stability and to avoid unnecessary control currents. However, non-contacting transducers commonly used to measure centerline displacement of rotating shafts are subject to measurement errors due to sensor runout. Although a direct measurement of geometric axis position is desired, these sensors measure the gap distance between a reference position and the shaft surface and are subject to errors caused by surface defects within the target area.

This thesis investigates the behavior of AMB control systems by nonlinear analysis and evaluates a novel position sensor to improve bearing performance by reducing runout error in the position signal. In Chapter II, sensor runout reduction is evaluated for a circular array of eddy current transducers by numerical simulation and by testing on a prototype 8-sensor array. Equations are developed to predict runout and synchronous measurement error in the position signal after individual sensor failures. In Chapter III, nonlinear frequency response behavior of a homopolar radial magnetic bearing is studied using numerical integration to identify stable orbital equilibrium states and a shooting algorithm is used to determine unstable rotor orbits and Floquet multipliers. Poincaré maps and bifurcation diagrams are used to characterize quasiperiodic rotor oscillations near nonlinear resonance. The information gathered in this study will help improve magnetic bearing performance through a better understanding of nonlinear magnetic bearing frequency response and provides a method to improve controllability by removing runout disturbances from the feedback path.

1.2 LITERATURE REVIEW

Rejection of periodic disturbances in magnetic bearing position sensor systems has been studied for both unbalance compensation and sensor runout reduction. While unbalance compensation requires filtering the sensor signal at the spin frequency, runout reduction requires filtration of both synchronous components and higher harmonics of running speed. Unbalance compensation techniques were developed to allow the rotor to spin about its inertial axis rather than its geometric axis if sufficient clearance is allowed. This capability provides an advantage over traditional roller bearings since unbalance vibrations are not transmitted to the housing. Runout reduction techniques were developed to provide a clean displacement signal representative of actual rotor position alone. In AMB control systems, sensor runout noise present in the feedback loop is passed on to the controller, causing unnecessary control currents and undesirable high frequency rotor motion. This closed-loop problem makes many open-loop designed runout reduction techniques insufficient for magnetic bearing applications. Although the intended goals of unbalance compensation and runout reduction differ, similar techniques have been used to solve both problems.

Elimination of synchronous displacement signal components has been accomplished by many researches using various methods. Knospe [1] examined the performance of notch filters installed between the sensor and controller for rejection of synchronous signals. To address the problems of phase-induced instability caused by these open-loop filters, Herzog [2] proposed a generalized notch filter which allowed arbitrary pole placement for decentralized operation. These filtering methods were effective only for a narrow speed range and examined only unbalance excitation at the spin frequency.

Alternative approaches to disturbance rejection involve adaptive feedforward techniques in which compensation signals are injected into the control loop to cancel or reduce the effect of the disturbance. These adaptive methods are categorized by the techniques used to determine the appropriate compensation signal. Adaptive runout compensation was first documented by Bently Nevada Corporation [3] by storing a

measured waveform recorded during slow-roll operation to characterize total runout without the contribution of inertial vibration. Useful displacement data results from subtracting the stored waveform from measured vibration signals. This method relied on the assumption that total runout is invariant for all operating conditions. To identify in-situ runout, Kim and Lee [4] used an extension of the influence coefficient method for two-plane rotor balancing to determine Fourier coefficients of the disturbance signal for a perfectly balanced rotor. Setiawan et. al. [5,6,7] used an adaptive approach based on the Lyapunov stability criterion to characterize the disturbance for both unbalance and sensor runout compensation. In this method, the disturbance is estimated and automatically updated using a feedback scheme until the estimate converges. Two algorithms were considered, one for runout cancellation alone and another for cancellation of both runout and mass unbalance.

Separation of unbalance vibration and synchronous runout signals is necessary because both disturbances occur at the same frequency. The extended influence coefficient method circumvented this problem by assuming a perfectly balanced rotor so that synchronous disturbances were due solely to runout. Other researchers developed ways to isolate synchronous runout from mass unbalance. To identify the contribution of unbalance, Setiawan et. al. characterized the displacement signal at two different rotor speeds [6] and later isolated unbalance disturbance by bias current excitation [7]. By removing unbalance effects from the runout compensation signal, the rotor can be spun about its geometric rather than its inertial axis.

Although adaptive compensation of periodic disturbances has been proven to successfully remove runout from the sensor signal, such methods are computationally intensive. Calculation time for adaptive algorithms introduces potentially destabilizing phase lag into the feedback loop. Two novel sensing systems have been proposed that utilize multiple sensors to reduce runout disturbances at the sensor level rather than in the controller. These sensing systems require amplification and summation of individual sensor outputs to produce independent position signals. Chapman [8] introduced a cylindrical capacitive sensor that eliminates even runout harmonics by geometric

averaging. Ahn and Han [9] altered the angular size of each capacitive sensor segment to remove the third harmonic and showed that a capacitive sensor having n equal sensing pairs could remove all but the $(2kn\text{-}1)$ and $(2kn\text{+}1)$ harmonics of runout. In a similar study of a circular array of multiple eddy current probe-type transducers, Li [10] showed that the weighted sum of n individual sensor outputs could eliminate harmonics from 2 to n-2 of the fundamental set. Li's sensor array is robust to individual sensor failures after modification of the weighting matrix. The sensor array is described in greater detail in Chapter II of this thesis.

Nonlinearities in rotordynamic systems have been studied extensively by many researchers. In rotordynamics, nonlinear response is often caused by shaft support structures such as fluid-film, roller, journal and magnetic bearings used to control unbalance vibrations. Magnetic bearings are nonlinear supports due to the quadratic relationship between coil current and magnetic forces. Maslen et al. [11] showed that magnetic bearings can produce rotor forces in an arbitrary direction using bias linearization. With this technique, linear control of the nonlinear AMB system is achieved by bias flux supplied either by permanent magnets or by biased coil currents. While such linear control techniques are able to stabilize the rotor and control unbalance vibrations, magnetic bearings exhibit nonlinear response characteristics that must be understood to improve performance and extend operating limits.

Extensive research has been performed to understand the nonlinear behavior of heteropolar magnetic bearings. Chinta and Palazzolo [12,13] used numerical integration and trigonometric collocation to locate periodic orbits and applied Floquet theory to determine their local stability and bifurcation behavior. Jumps and subharmonic response were investigated by varying rotor speed, imbalance and weight in this study. Ji and Hansen [14] used the method of multiple scales to determine steady state amplitude and phase relationships of nonlinear vibrations. Here, jumps to stable periodic orbits by saddle node bifurcation were illustrated by frequency response curves. Amplitude modulated response was obtained for increased forcing amplitudes by Hopf bifurcations.

Homopolar magnetic bearings are a more recent development in AMB technology. While nonlinearities in homopolar bearings have not been fully addressed in the literature, several researchers have studied other characteristics of their operation. Kasarda et. al. [15] investigated the reduced power losses of homopolar bearings due to hysteresis, eddy currents and windage by theory and experimentation. Kim [16] furthered these results by detailed magnetic field modeling of flux paths to characterize eddy current losses. Na [17] and Li [10] developed fault tolerant homopolar magnetic bearings using a current distribution matrix that was reconfigurable upon pole failure. The only nonlinear study of homopolar bearings by Kenny [18] focused on methods to reduce power losses due to electromagnetic nonlinearities. The present research develops governing nonlinear equations for a radial homopolar magnetic bearing and for a linearized magnetic bearing model using bias linearization principles. Frequency response curves for the nonlinear magnetic support force are compared to the linearized model. Bifurcations near nonlinear resonance frequencies are analyzed by Floquet theory and subsequent rotor behavior. These bifurcations result in sudden amplitude jumps and quasiperiodic rotor oscillations.

1.3 RESEARCH OBJECTIVES

The purpose of the present work is to improve understanding and performance of active magnetic bearing control systems. This thesis focuses on two different aspects of magnetic bearings that require further analysis. The first involves reduction of periodic disturbances caused by sensor runout in the position feedback signal. The method investigated attempts to remove runout harmonics from the sensor signal while adding fault tolerance of individual sensor failures. Second, nonlinear response of homopolar magnetic bearings is studied to identify locally stable and unstable periodic orbits and to characterize the effects of rotor speed changes on steady state response. Results obtained through these investigations can be used to operate magnetic bearings at greater speeds and to support larger and more imbalanced rotors.

1.4 ORGANIZATION

Chapter II analyzes the performance of the circular sensor array for reduction of runout disturbance in the magnetic bearing position sensor system. The sensor array is described in detail and two approaches for fault tolerance are explained. For one of these approaches, numerical simulations are used to simulate individual sensor failures and the amplitudes of signal harmonics are compared to analytical predictions for different failure configurations. A prototype drive circuit is developed to verify operational theory and an 8-sensor array is tested to compare performance to a commercial position transducer system.

Chapter III explores the nonlinear behavior of homopolar magnetic bearings using numerical methods. Nonlinear equations of motion are developed to model a 6 pole homopolar magnetic bearing configuration. These equations are used to form a linear model based on bias linearization principles. Orbital equilibrium amplitudes of the nonlinear system are determined using direct numerical integration for stable orbits and using a shooting algorithm for unstable rotor orbits. These results are compiled as frequency response curves that are contrasted with the linear model for increasing and decreasing rotor speeds. At frequencies near nonlinear resonance, quasiperiodic rotor orbits are characterized using bifurcation diagrams and Poincaré maps.

Chapter IV summarizes the results from the sensor array analysis and nonlinear study. These results are used to support conclusions that can be used to improve performance of magnetic bearing control systems and to select optimal operating conditions. Future research in these areas is suggested for further study.

1.5 ORIGINAL CONTRIBUTIONS

- Simulate output of an n-sensor array for a rotor with a defined runout pattern in the time and frequency domains. Determine amplitude attenuation of runout harmonics achieved by the ideal sensor array. Characterize effects of single and opposing pair sensor failures on array outputs.
- Test a prototype 8-sensor array to determine actual sensitivity, linearity, noise amplitude, bandwidth, and runout reduction performance.
- Determine stable and unstable orbital equilibrium states of a homopolar radial magnetic bearing using numerical integration and shooting.
- Develop amplitude and phase frequency response curves for a homopolar radial magnetic bearing with proportional control gains that result in softening spring behavior.
- Analyze bifurcations of stable equilibrium orbits by Floquet theory using numerically determined Floquet multipliers, Poincaré maps and bifurcation diagrams.

CHAPTER II

CIRCULAR SENSOR ARRAY

2.1 INTRODUCTION

A vital yet often overlooked component of magnetic bearing control systems is the sensor used to monitor rotor position. Sensor signals are used by the AMB controller to determine the control currents required to improve performance or stabilize the rotor. Ideally, signals generated by the sensing system should provide an exact measurement of system states. In practice, noise enters the control system through the sensors in various forms that degrade controller performance and can lead to instability. In rotordynamic applications, sensor noise disturbance can often be attributed to runout. This chapter describes the development of a fault-tolerant circular array of eddy current proximity probes to measure rotating shaft deflection with reduced runout error. The objective of the sensor array is to reduce runout noise in the sensor signal and provide fault tolerance of individual sensor failures.

The sensors commonly used to measure displacement of a rotating shaft are non-contacting transducers that use eddy currents to measure the air gap between the rotor surface and probe tip. Since the shaft centerline is not measured directly, the sensor signal includes measurement error called sensor runout. There are many causes of sensor runout that can arise from differences in shaft geometry, alignment, and material inhomogeneity. Runout can be divided into two categories: mechanical runout and electrical runout. Mechanical runout is the result of changes in the distance between the probe tip and rotor surface not caused by inertial vibratory forces. This error is caused by shaft imperfections such as non-circular cross-sections, rotor alignment problems, and surface roughness. Electrical runout results from changes in the measured displacement signal due to inhomogeneous electromagnetic properties around the shaft circumference. These effects become more pronounced the closer defects are to the sensing surface. Shaft coatings and surface treatments can significantly alter material inductance, limiting the ability to form eddy currents. Other common causes of electrical

runout are material defects such as voids, inclusions or residual magnetic fields near the shaft surface. Both mechanical runout and electrical runout are detected by eddy current transducers. This total runout error results in sensor signals that can be represented by a Fourier series expansion composed of harmonics of the running speed.

$$g(t) = A_0 + \sum_{k=0}^{\infty} \left[A_k \cos(k\omega t) + B_k \sin(k\omega t) \right]$$

The total sensor signal is the summation of vibration response to rotor unbalance, environmental noise and runout disturbance. Synchronous vibration control using magnetic bearings commonly employs PD gains applied to the combined sensor signal, resulting in unnecessary control currents at harmonics of spin frequency. Filtering methods to remove runout from the sensor signal are not effective in many AMB control systems due to phase lag and limited speed range. Adaptive methods require potentially destabilizing computation time and additional hardware to remove runout. One attractive alternative to these approaches is to use a weighted sum of individual sensor outputs from a circular sensor array to remove certain runout harmonics.

This chapter explores the sensor array method of runout reduction by analysis, numerical simulation and by testing of a prototype system. Amplitude attenuation of runout harmonics is predicted using an analytical expression. Actual amplitudes of array output harmonics are verified by idealized simulations of an unfailed 8-sensor array and 16-sensor array. Fault tolerance of individual sensor failures is investigated using numerical simulations of the 8-sensor and 16-sensor arrays for certain single and double probe failures. To evaluate actual sensor array performance for the unfailed case, a prototype 8-sensor array is built and tested. Design considerations for development of the prototype 8-sensor array are explained by analysis of the working principles of eddy current transducers. Finally, testing of the prototype sensor array is performed on two different test fixtures and compared to a similar commercial transducer system using only two probes.

2.2 DESCRIPTION OF SENSOR ARRAY

The sensor array analyzed in this thesis is made up of an even number of identical eddy-current proximity probes equally spaced around the rotor diameter. All probes are in the same plane whose normal is parallel to the target rotor axis of rotation. This ensures that individual probes measure the same circumferential track at different angular positions. Each probe is set to the same nominal gap distance when the rotor is at geometric center. In this way, any one point on a perfectly balanced rotating shaft produces the same output at each probe location. Probes are aligned so that their axes intersect at a point coincident with the geometric center of the magnetic bearing assembly. This configuration is shown using 8 equally-spaced probes in Figure 2.1.

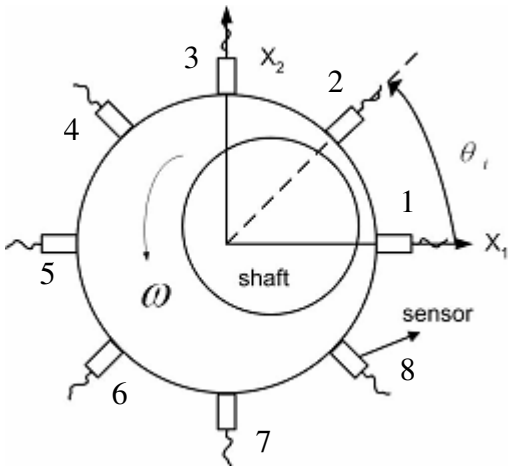

Figure 2.1 Circular 8-sensor array [10]

Within its operating range, probe voltage is a linear function of the air gap between the probe tip and the target surface. Sensor sensitivity (ξ) describes this proportional change in sensor voltage with gap distance. For commercial eddy current transducers, sensitivity is nearly constant for air gaps from 10 to 90 mils [19]. It is assumed that gap distance always falls within these limits so that the voltage output of each probe in an *n*-sensor array can be described by

$$V_s = \xi \cdot d_{gap} \tag{1}$$

where V_s and d_{gap} represent n-by-1 vectors of individual sensor voltages and gap distances, respectively.

Radial magnetic bearing control systems require two independent displacement signals for the two orthogonal control directions. When more than two sensors are used to measure rotor displacement, individual sensor outputs must be manipulated to provide these two independent signals. Li [10] showed that n individual sensor voltages can be used to determine these two displacement signals using an appropriate linear mapping called the weighting gain matrix (WGM). This mapping can be written

$$V_{SA} = \begin{bmatrix} v_{x1} \\ v_{x2} \end{bmatrix} = \xi TFd \tag{2}$$

where T is the WGM and F describes the failure state of the sensors in the array. The 2-by-n WGM is determined by solving a set of linear constraint equations for the failure state of the sensor array. Failure state is indicated by an n-by-n diagonal matrix of ones and zeros with zero entries corresponding to the failed sensors. Simulation results showed that an n-sensor array using the appropriate WGM can successfully remove runout harmonics from 2 to n-2 of the fundamental harmonic set when all sensors are operational.

The sensor array provides an additional benefit in the form of fault-tolerance of sensor failures. Fault-tolerance is desirable in magnetic bearing control systems because component failures can be catastrophic at high speeds. Recently, magnetic bearings have been considered for flywheel energy storage systems used in satellites, where component loss can cause mission failure. Traditional approaches to position sensing in magnetic bearings cannot accommodate individual sensor failures. The sensor array improves on these approaches by maintaining reliability in the presence of certain sensor failure states.

There exist 2^n-1 possible sensor failure combinations, each with a unique WGM that may be used to eliminate runout harmonics. These WGMs can be stored in a look-up table and the appropriate WGM swapped in when a failure occurs. Li examined this

swap-in approach (SIA) and showed that reliability of the sensor array increases with the number of sensors. This reliability analysis considered two criteria for failure of the sensor array in the presence of individual sensor faults. The sensor array was considered successful if both the error in output invariance and magnitude of the k^{th} harmonic of runout fall within tolerances dictated by the robustness of the controller. The error in output invariance was described in [10] by the 2-by-2 matrix

$$E = TF\Theta - I \tag{3}$$

where Θ is an n-by-2 transformation matrix from rotor position to probe gap distances. This error describes the relationship between actual and measured rotor position at any instant in time. The magnitude of the k^{th} harmonic sensed along the j^{th} control direction was described in [10] by

$$\gamma_{jk} = \sqrt{\left(\sum_{i=0}^{n} \cos(k\theta_i) T_{ji} F_{ii}\right)^2 + \left(\sum_{i=0}^{n} \sin(k\theta_i) T_{ji} F_{ii}\right)^2} \qquad j = 1, 2 \tag{4}$$

where θ_i represents the angle from the positive x1 control direction to the i^{th} sensor location. This expression reduces to unity for $k = 1$ and $k = n$-1 and to zero for $k = 2$ to $k = n$-2 when all sensors are operational. This magnitude represents the relative amplitude of signal harmonics in the sensor array outputs as compared to the frequency content of a single sensor signal.

The swap-in approach requires extensive hardware to detect sensor failures, store WGMs, and load the proper WGM after failure occurs. The present analysis is intended to determine the effectiveness of using the no-swap-in approach (NSIA), where a single WGM is used regardless of the failure state. The WGM chosen for this study corresponds to the no-failure state of an n-sensor array. Using this strategy, the contribution of each sensor in the 8-sensor array to x1 (j=1) and x2 (j=2) array output signals can be shown by the unfailed WGM

$$T_8 = \begin{bmatrix} 0.2500 & 0.1768 & 0 & -0.1768 & -0.2500 & -0.1768 & 0 & 0.1768 \\ 0 & 0.1768 & 0.2500 & 0.1768 & 0 & -0.1768 & -0.2500 & -0.1768 \end{bmatrix} \tag{5}$$

regardless of the failure state of the sensors in the array. Similarly, the 16-sensor array possesses a unique WGM for the unfailed state shown by

$$T_{16} = \begin{bmatrix} 0.1250 & 0.1155 & 0.0884 & 0.0478 & 0 & -0.0478 & -0.0884 & -0.1155 \\ 0 & 0.0478 & 0.0884 & 0.1155 & 0.1250 & 0.1155 & 0.0884 & 0.0478 \\ -0.1250 & -0.1155 & -0.0884 & -0.0478 & 0 & 0.0478 & 0.0884 & 0.1155 \\ 0 & -0.0478 & -0.0884 & -0.1155 & -0.1250 & -0.1155 & -0.0884 & -0.0478 \end{bmatrix} \tag{6}$$

to scale individual sensor voltages for all failure configurations. The weighting gain matrix can easily be determined for any generalized *n*-sensor array using the expressions

$$\begin{aligned} T_{1,i} &= \frac{2}{n}\cos\theta_i \\ T_{2,i} &= \frac{2}{n}\sin\theta_i \end{aligned} \tag{7}$$

for each row when all sensors are operational. In the swap-in approach, individual WGM entries must be adjusted from this ideal case to compensate for sensor failures. However, additional hardware and memory requirements make this approach difficult to implement. The no-swap-in approach studied in this thesis requires less hardware support, but results in measurement errors when individual sensors fail. This analysis quantifies the NSIA measurement error resulting from sensor runout for different failure configurations.

Performance of the sensor array using the NSIA is studied by analysis and numerical simulation of various sensor failures and by prototype testing on a spinning rotor. This research shows that the sensor array can reduce runout error for both ideal and actual conditions. Runout error is judged by the amplitude of displacement signal harmonics with and without the sensor array in different failure modes. Measurement error as a result of sensor failures using the NSIA is judged by the amplitude of synchronous and DC harmonics compared to the unfailed case. It will be shown that this measurement error can be predicted if the failure location is known and then corrected by applying an amplitude adjustment factor.

2.3 NUMERICAL SIMULATION AND RESULTS

The runout reduction performance of an ideal sensor array is evaluated by numerical simulation for selected possible failure configurations. This simulation uses an arbitrary runout profile to generate individual sensor voltages with frequency-rich runout disturbance. Array output voltages are obtained from individual sensor voltages using the NSIA by applying the no-failure WGM for all failure combinations. Performance of the sensor array for each case is judged by the amplitudes of the first n harmonics of each sensor array output in comparison to the signal from only one sensor. The effect of sensor failure on the DC component of array output is analyzed to prevent DC shifts. Next, an expression is derived to predict the amplitudes of output harmonics after sensor failure. Simulations of single sensor failures at different angular positions are performed and compared to analytical predictions for an 8-sensor array and for a 16-sensor array. Finally, failure of opposing sensor pairs is simulated and compared to analytical results for both the 8-sensor and 16-sensor arrays.

Several assumptions must be made to facilitate analysis and simulation and to isolate runout effects. The model sensor array studied here is perfectly constructed according to the above description using ideal components. The assumption of ideal components results in identical sensitivity, bandwidth, and behavior of all sensors in the array. Sensor failure is assumed open-circuit so that failed probe voltage is identically zero. Ideal construction means that all sensors record the same voltage when a perfect rotor is centered in the array. For small assumed motions, curvature effects of the sensing surface are not considered. In addition, measurement noise due to electromagnetic interference, sensor cross-talk and material reluctance is neglected in this simulation. In the model, rigid probe mounting to an isolated support structure is assumed so that measurements may be considered as absolute rather than relative displacements. Furthermore, it is assumed that the rotor is perfectly balanced and experiences no lateral vibration so that signal variations are due solely to runout.

To evaluate disturbance rejection by the sensor array, a sample runout signal containing known harmonics is generated by the simulation software. A desirable test

pattern contains equal amplitude harmonics so that the relative attenuation of each harmonic can be verified. A rotational frequency of 10 Hz is assumed for generation of these harmonics, though this frequency has no other effect on the idealized array since bandwidth effects are neglected. To generate such a signal, *n* sinusoidal functions with integer multiples of the fundamental frequency are summed using MATLAB to simulate the runout sensed by a single probe. Each sinusoid is assumed to have an amplitude of 2.0 mils and is phase-shifted to create a smooth signal when all harmonics are combined. Each probe is assumed to have a constant sensitivity of 200 mV/mil. A simulation of the 8-harmonic runout signal as recorded by a single sensor is shown with its frequency spectrum in Figure 2.2. Runout reduction performance of the sensor array is compared to this single sensor signal in all numerical simulations.

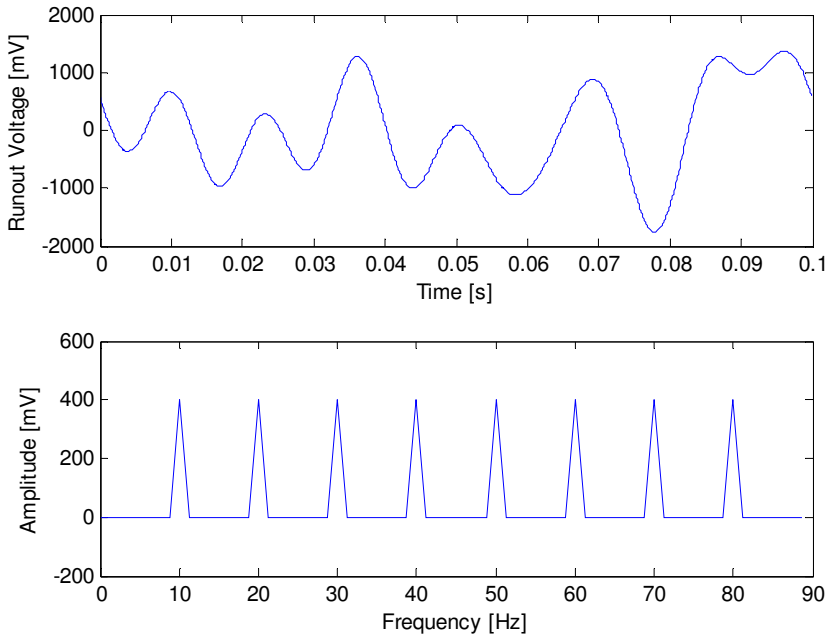

Figure 2.2 Runout signal used for numerical simulation in time and frequency domains

Since the simulation assumes a perfectly centered and balanced rotor, the signal observed by each sensor in the array is simply a phase shifted version of this runout pattern. These *n* sensor signals are stored in an *n*-by-*t* array of probe voltages where *t* is the length of the time record. This array is multiplied with the WGM according to (2)

for every possible combination of one and two-sensor failures to produce sensor array outputs for the x1 and x2 control directions at each time step. Frequency content of sensor array output signals is determined using a discrete Fourier Transform (DFT) for each failure case.

To simplify the DFT algorithm, the number of samples in the time record is selected as a power of 2. The total number of samples in the time record is dictated by the desired frequencies to be observed. In the simulation, these desired frequencies are exactly known since the signal was generated by summing individual harmonics. To observe the synchronous component of runout, the period of the time record must be at least twice the fundamental period of rotation. To observe the n^{th} harmonic of runout, the number of samples in the time record must be at least $2n$. This simulation considers n full rotations with 2^{12} samples per rotation to exceed the frequency limits and ensure sufficient resolution in the time domain for the 8-sensor and 16-sensor arrays.

The effect of various sensor failures is examined for both an 8-sensor and a 16-sensor array. These configurations are selected because equal probe spacing results in two probes located along each measurement direction (on-axis) with additional probes located between the two orthogonal measurement axes (off-axis). This allows both direct and indirect measurements of rotor position and provides redundancy in case of failure. For rotor diameters less than 3 inches, more than 16 standard eddy-current probes will not easily fit in a circular array with the required gap distances. A numbering convention is adopted to reference each sensor in the generalized array. The sensors are numbered counter-clockwise from 1 to n, beginning with the sensor along the positive x1-direction as shown in Figure 2.1.

This analysis considers the no-swap-in approach (NSIA) in which a single WGM is used for all failure states. This WGM is optimized for best performance during the no-failure state using (7). As predicted by Li [10], simulation results show that the unfailed sensor array will successfully remove runout harmonics 2 to n-2 of the fundamental set using this WGM. Simulated single axis output of the unfailed 8-sensor

array is shown with its frequency spectrum in Figure 2.3 when the WGM in (5) is applied to individual sensor signals.

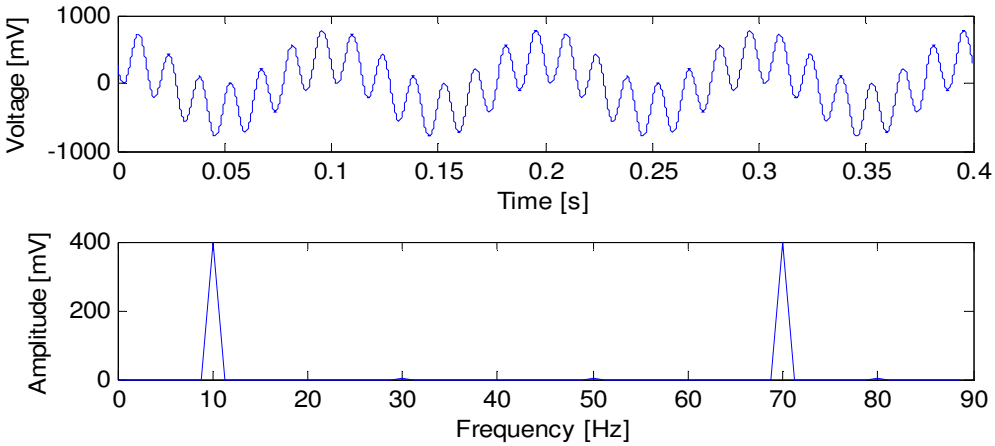

Figure 2.3 Attenuation of runout harmonics using 8-sensor array, no failures

In comparison to Figure 2.2, the runout-compensated output harmonics of the unfailed 8-sensor array represent a vast improvement over the total runout signal as sensed by a single sensor. Harmonics 2 to 6 are substantially reduced for this case below 10^{-12} mV. By eliminating these intermediate harmonics at the sensor level, magnetic forces generated by the AMB system may approach the pure synchronous response necessary to efficiently control unbalance vibration. This simulation is later confirmed by experimentation on a prototype sensor array with no sensor failures.

As described previously, a fundamental advantage of the sensor array for runout reduction is fault-tolerance to individual sensor failures. The swap-in approach (SIA) accommodates sensor failures by updating the WGM used to map individual sensor outputs to two independent control signals. The present analysis (NSIA) explores the effects of single sensor failures on array outputs when the original WGM is applied for all failure states. Desirable features of the total sensor signal after failure include maximum attenuation of super-synchronous harmonic amplitudes and invariance of the synchronous and DC signal components. While these desired signal attributes are easily attained using the SIA, probe failures limit array performance using the NSIA. Sensor

array performance in meeting these competing requirements is evaluated in relation to single sensor output by the metrics of runout error and measurement error, respectively.

Sensor failures limit runout reduction ability of the sensor array when the WGM is not swapped to compensate for individual probe loss. In this analysis, runout error is measured by the amplitude of super-synchronous harmonics of sensor array outputs relative to single sensor measurements without runout compensation. The goal of the sensor array is to reduce runout error to negligible levels for all signal harmonics. As shown previously, a fully functioning sensor array can completely remove harmonics 2 to n-2 of the fundamental set to give zero runout error for these harmonics. Sensor failure analysis will show that the sensor array can reduce runout error even with some sensors failed. Runout error is shown for each fundamental harmonic in each output signal in the following analysis of sensor failures.

Synchronous signal components should not be altered by the sensor array because the array is unable to differentiate between synchronous runout and useful vibration data without using adaptive methods. In addition, the DC component of sensor array output provides a measure of average rotor position that must be maintained near the magnetic bearing center to ensure symmetric magnetic forces. With the NSIA sensor array, sensor failure alters these lower signal harmonics as well. This change in synchronous and DC signal harmonics after sensor failure is termed measurement error. Measurement error is quantified by the amplitude of synchronous and DC signal components of sensor array output relative to single sensor signals. This error is assumed to be zero for the ideal unfailed sensor array but must remain within allowable tolerances after individual sensor failures. These allowable tolerances are dictated by the robustness of the AMB controller and by permissible rotor motion. In the following sensor failure analysis, measurement error is shown for synchronous and DC harmonics in each output signal. It will be shown that DC measurement error can be lowered by controlling probe bias voltage and that synchronous amplitude can be preserved after sensor failures by application of an amplitude adjustment factor that varies with failure location.

The DC measurement error after sensor failure can be reduced by minimizing the difference between nominal gap voltage and failed probe voltage. Commercial eddy-current transducers are biased to a non-zero negative voltage at the nominal gap distance. This negative bias is sufficient for single sensor measurements, but becomes problematic in the sensor array. When a sensor fails by open-circuit fault, its output becomes zero rather than the nominal gap bias voltage. It is assumed that all probe failures can be classified as open-circuit or that probe voltage can be zeroed upon failure. The resulting difference in individual probe voltages results in a large DC shift of the array output after failure as shown in Figure 2.4.

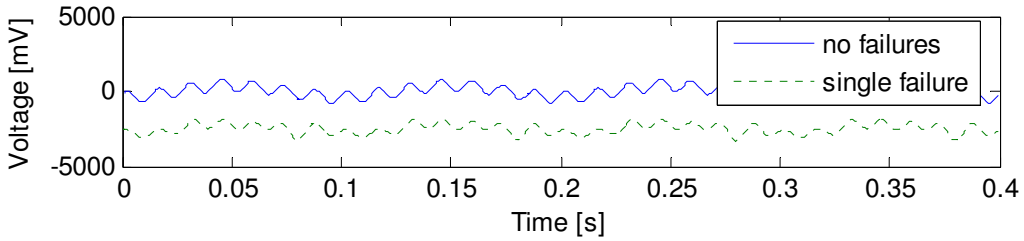

Figure 2.4 DC shift using 8-sensor array, sensor 1 failed, non-zero bias

This problem can be circumvented by ensuring that failed sensor voltage is close to the nominal gap voltage of an individual sensor. In this way, failed sensors have less impact on the DC component of array outputs when the actual position of the rotor is near the bearing center. This gap bias can be accomplished either by biasing all probes to zero at the nominal gap distance or by introducing circuitry to substitute nominal gap voltage upon probe failure. The former method is used for the following simulations of sensor failures to prevent large DC measurement errors.

In this analysis of sensor failure effects using the NSIA, runout error and measurement error are shown for single and double probe failures in various failure configurations. Sensor failures are shown to cause a reduction in sensor array performance for all failure configurations. For each harmonic, the magnitude of the error terms is related to failed probe location and the number of sensors in the array. The 8-sensor array is studied first to characterize the effect of failed probe location on

array outputs for single failures. Next, the 16-sensor array is studied to show the effect of increasing the number of sensors in the array. Finally, selected double probe failures are simulated for both the 8-sensor and 16-sensor arrays. This analysis will show how runout error and measurement error are affected by sensor failures and provides a means to correct measurement error if it exceeds allowable tolerances.

In the ideal conditions of this simulation, the relative amplitude performance metrics of runout error and measurement error can be predicted using the k^{th} harmonic magnitude $\gamma_{j,k}$ described by (4). This magnitude reduces to zero for harmonics 2 to n-2 and equals one for harmonics 1 and n-1 when all probes are operational. After probe failures, the new magnitude of the k^{th} harmonic $\gamma_{j,k}^{F}$ is found by subtracting the contribution of each failed sensor from the no-failure magnitude $\gamma_{j,k}^{NF}$. Substituting the expression for the i^{th} WGM entry given in (7) into this difference for each control direction gives

$$\begin{aligned}
\gamma_{1k}^{F} &= \left\| \gamma_{k}^{NF} - \sqrt{\left(\sum_{n_F} \frac{2}{n} \cos(k\theta_i)\cos(\theta_i) \right)^2 + \left(\sum_{n_F} \frac{2}{n} \sin(k\theta_i)\cos(\theta_i) \right)^2} \right\| \\
\gamma_{2k}^{F} &= \left\| \gamma_{k}^{NF} - \sqrt{\left(\sum_{n_F} \frac{2}{n} \cos(k\theta_i)\,\sin(\theta_i) \right)^2 + \left(\sum_{n_F} \frac{2}{n} \sin(k\theta_i)\,\sin(\theta_i) \right)^2} \right\|
\end{aligned} \tag{8}$$

where n_F denotes the number of failed sensors. Expanding the sine and cosine products using trigonometric identities, these expressions can be greatly simplified for single sensor failures as

$$\begin{aligned}
\gamma_{1,k}^{F} &= \left\| \gamma_{k}^{NF} - \frac{1}{n}\sqrt{2 + 2\cos(2\theta)} \right\| \\
\gamma_{2,k}^{F} &= \left\| \gamma_{k}^{NF} - \frac{1}{n}\sqrt{2 - 2\cos(2\theta)} \right\|
\end{aligned} \tag{9}$$

where the second term represents single failure measurement error for $k = 1$ and runout error for $k > 1$. These magnitudes can be used to predict synchronous measurement error and runout error for any failure combination for an arbitrary n-sensor array using the

NSIA. This is verified by numerical simulation of selected sensor failure configurations on the 8-sensor and 16-sensor arrays for both single and double probe failures.

SINGLE SENSOR FAILURES

Single sensor failures result in lower synchronous amplitudes and less attenuation of runout harmonics in comparison to the unfailed array. Failure of the i^{th} sensor is simulated by setting the i^{th} diagonal entry in the F matrix to zero. Sensor array output voltages for the x1 and x2 control axes are determined according to (2) for all possible failure states. Frequency content of these independent position signals is determined by taking the DFT of each simulated voltage over n full shaft rotations using the runout profile previously described. The resulting fundamental harmonic amplitudes contained in each position signal are shown in Table 2.1 for sensor 1 failure in the 8-sensor array. Corresponding amplitudes for the no-failure case and predicted single failure amplitudes using (9) are also shown for reference.

Table 2.1 Harmonic amplitudes for 8-sensor array, sensor 1 failed

		j=1		**j=2**	
k	γ_k^{NF}	**simulation**	γ_{1k}^{F}	**simulation**	γ_{2k}^{F}
1	1.0	0.7498	0.7500	0.9998	1.0000
2	0	0.2499	0.2500	0.0000	0.0000
3	0	0.2501	0.2500	0.0000	0.0000
4	0	0.2499	0.2500	0.0000	0.0000
5	0	0.2501	0.2500	0.0000	0.0000
6	0	0.2501	0.2500	0.0000	0.0000
7	1.0	0.7493	0.7500	0.9990	1.0000

This data shows good correlation between predicted harmonic amplitudes and simulation results for sensor 1 failure. Differences between simulation results and calculated amplitudes can be attributed to the discrete representation of sensor voltages and truncation errors in the DFT algorithm. Note that failure of sensor 1 has no effect on the

x2 array output signal since the $T_{2,1}$ entry in the 8-sensor WGM is zero. Physically, the failed sensor is located at an angular position for which motion in the x2-direction cannot be detected. To show how certain sensor failures can affect both array outputs, harmonic amplitudes for the 8-sensor array are shown in Table 2.2 for sensor 2 failed.

Table 2.2 Harmonic amplitudes for 8-sensor array, sensor 2 failed

		j=1		**j=2**	
k	γ_k^{NF}	**simulation**	γ_{1k}^{F}	**simulation**	γ_{2k}^{F}
1	1.0	0.8837	0.8232	0.8837	0.8232
2	0	0.1767	0.1768	0.1767	0.1768
3	0	0.1769	0.1768	0.1769	0.1768
4	0	0.1767	0.1768	0.1767	0.1768
5	0	0.1769	0.1768	0.1769	0.1768
6	0	0.1768	0.1768	0.1768	0.1768
7	1.0	0.8830	0.8232	0.8830	0.8232

According to this simulation, failure of either sensor 1 or sensor 2 results in increased runout error and increased synchronous measurement error. In fact, failure of any one sensor has a similar effect on sensor array performance to differing degrees. These results can be generalized for single failure of any one sensor in an *n*-sensor array. Failure of any one sensor that lies along the x1 or x2 measurement axis will alter the position signal for that axis but will not affect the other array output signal. Failure of any one sensor that does not lie directly on a measurement axis will affect both array output signals. In order to understand how these off-axis sensor failures affect each array output signal, simulations of single sensor failures are performed for the 16-sensor array.

The 16-sensor array is useful for analysis of sensor failures that do not lie along a measurement axis because multiple probes are located between the x1 and x2 directions. This allows simulation of single sensor failures that have unequal effects on each array output signal. For this simulation, the runout signal is modified to include 16 equal

amplitude harmonics. As before, runout harmonics are modeled with 400 mV amplitudes and the rotor is assumed to spin at a frequency of 10 Hz. Single axis output of the unfailed 16-sensor array with this modified runout profile is shown with its frequency spectrum in Figure 2.5.

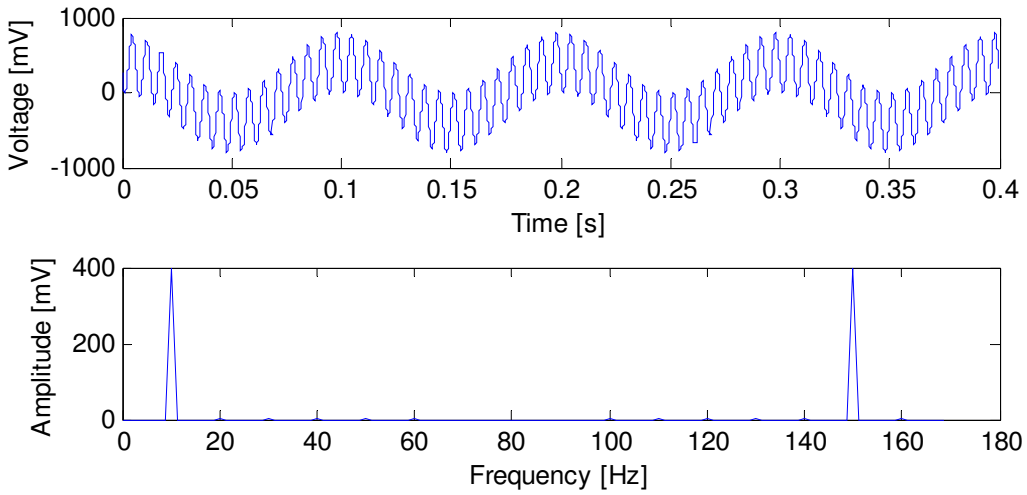

Figure 2.5 Attenuation of runout harmonics using 16-sensor array, no failures

This shows that the 16-sensor array also removes harmonics of runout from 2 to *n*-2 when all sensors are operational. Elimination of additional harmonics from the sensor signal is one benefit of increasing the number of sensors in the array. Other advantages of increasing the quantity of sensors are found by examination of array outputs after single sensor failure.

As shown by (9), the change in harmonic amplitudes after single sensor failure is inversely proportional to the number of sensors in the array, resulting in less measurement and runout error for the 16-sensor array compared to the 8-sensor array. This is shown for failure of sensor 1 of the 16-sensor array in Table 2.3.

Table 2.3 Harmonic amplitudes for 16-sensor array, sensor 1 failed

		j=1		j=2	
k	γ_k^{NF}	**simulation**	γ_{1k}^{F}	**simulation**	γ_{2k}^{F}
1	1.0	0.8744	0.8750	0.9994	1.000
2	0	0.1249	0.1250	0.0000	0.000
3	0	0.1250	0.1250	0.0000	0.000
4	0	0.1250	0.1250	0.0000	0.000
5	0	0.1251	0.1250	0.0000	0.000
6	0	0.1251	0.1250	0.0000	0.000
7	0	0.1248	0.1250	0.0000	0.000
8	0	0.1249	0.1250	0.0000	0.000
9	0	0.1249	0.1250	0.0000	0.000
10	0	0.1250	0.1250	0.0000	0.000
11	0	0.1253	0.1250	0.0000	0.000
12	0	0.1249	0.1250	0.0000	0.000
13	0	0.1251	0.1250	0.0000	0.000
14	0	0.1250	0.1250	0.0000	0.000
15	1.0	0.8735	0.8750	0.9983	1.000

For sensor 1 failure in the 16-sensor array, simulation results agree well with predicted values for each harmonic. As expected, the synchronous measurement error is lower for the 16-sensor array than for the 8-sensor array when the same sensor is failed. Similarly, runout error is reduced for single sensor failure in the 16-sensor array. Since sensor 1 is located along the x1 measurement axis, failure of this sensor does not affect the x2 position signal. To study failure effects on both array output signals, an off-axis sensor must be failed.

In contrast to the 8-sensor array, there are 3 off-axis sensors between each on-axis sensor of the 16-sensor array. After failure of one of these off-axis sensors, the change in harmonic amplitudes contained in each array output signal is related to the location of the failed sensor. This is shown for sensor 2 failure in the 16-sensor array in Table 2.4. Note that sensor 2 is in a different location for the 16-sensor array than for the 8-sensor array.

Table 2.4 Harmonic amplitudes for 16-sensor array, sensor 2 failed

		j=1		j=2	
k	γ_k^{NF}	**simulation**	γ_{1k}^{F}	**simulation**	γ_{2k}^{F}
1	1.0	0.8938	0.8845	0.9821	0.952
2	0	0.1154	0.1155	0.0478	0.048
3	0	0.1155	0.1155	0.0478	0.048
4	0	0.1155	0.1155	0.0478	0.048
5	0	0.1156	0.1155	0.0479	0.048
6	0	0.1155	0.1155	0.0479	0.048
7	0	0.1153	0.1155	0.0478	0.048
8	0	0.1154	0.1155	0.0478	0.048
9	0	0.1154	0.1155	0.0478	0.048
10	0	0.1155	0.1155	0.0478	0.048
11	0	0.1158	0.1155	0.0480	0.048
12	0	0.1154	0.1155	0.0478	0.048
13	0	0.1156	0.1155	0.0479	0.048
14	0	0.1155	0.1155	0.0478	0.048
15	1.0	0.8929	0.8845	0.9810	0.952

Since sensor 2 in the 16-sensor array is located near the x1 measurement axis, failure of this sensor has a greater effect on runout and measurement error in the x1 direction. In fact, failure of sensor 4 in the 16-sensor array has the same effect on the x2 signal harmonics as sensor 2 failure has on the x1 signal harmonics. Failure of sensor 3 in the 16-sensor array impacts both array outputs equally because this sensor is located at the same angle from each measurement axis.

These simulations show good correlation between predicted values of the k^{th} signal harmonic and ideal sensor array operation for single sensor failures. Such failures result in increased runout and measurement error for all failure configurations. The magnitude of these error terms in each array output signal is related to failure location and the number of sensors in the array. Although sensor failure location cannot be selected in practice, errors can be reduced by increasing the number of sensors. If single sensor failure still results in measurement error that exceeds allowable tolerances,

synchronous amplitude can be adjusted after sensor failure to provide a better measurement of actual rotor vibrations.

Since single sensor failures result in lower measured amplitudes of synchronous vibration, actual rotor vibration may be larger than the sensor array indicates. In applications where this difference cannot be tolerated, synchronous amplitude can be adjusted to correct measurement error if the failure location is known. This amplitude adjustment factor is applied to the erroneous array outputs as

$$v_{xj} = \frac{\gamma_{j,1}^{F}}{\gamma_{j,1}^{NF}} v'_{xj} \tag{10}$$

where v'_{xj} is the erroneous sensor array position signal. For the synchronous $k = 1$ harmonic, this amplitude adjustment factor becomes

$$\begin{aligned} \frac{\gamma_{1,1}^{F}}{\gamma_{1,1}^{NF}} &= \frac{1}{n}\sqrt{2+2\cos(2\theta_i)} \\ \frac{\gamma_{2,1}^{F}}{\gamma_{2,1}^{NF}} &= \frac{1}{n}\sqrt{2-2\cos(2\theta_i)} \end{aligned} \tag{11}$$

for the x1 and x2 measurement directions. To calculate this adjustment factor, failure detection circuitry is required to locate the failed sensor. Although the primary advantage of using the NSIA for sensor failures is reduced hardware and memory requirements, the memory space needed to store these adjustment factors is less than the size of the different WGMs used in the SIA. In addition, implementing the amplitude adjustment factor would only require replacement of 2 values rather than the $2n$ values that would make up a new WGM. Other than this additional circuitry, the major drawback to synchronous amplitude adjustment is increased runout error compared to the unadjusted array output signals. This is shown for the 8-sensor array with sensor 2 failure after amplitude adjustment in Table 2.5.

Table 2.5 Harmonic amplitudes for 8-sensor array, sensor 2 failed, amplitude adjusted

k	γ_k^{NF}	**unadjusted**	$\gamma_{1k}^{F} = \gamma_{2k}^{F}$	**adjusted**
1	1.0	0.8837	0.8232	1.0735
2	0	0.1767	0.1768	0.2147
3	0	0.1769	0.1768	0.2148
4	0	0.1767	0.1768	0.2147
5	0	0.1769	0.1768	0.2149
6	0	0.1768	0.1768	0.2148
7	1.0	0.8830	0.8232	1.0727

This simulation shows a small increase in runout error and a decrease in measurement error after synchronous amplitude is adjusted for sensor 2 failure. Relative amplitude of the synchronous sensor signal is not exactly unity due to slight differences in the predicted and actual values. Despite this difference, the amplitude-adjusted sensor array output provides a much better indication of actual rotor vibration than the unadjusted output after single sensor failure.

DOUBLE SENSOR FAILURES

The concepts shown for single sensor failures can be extended to describe the effects of multiple sensor failures. Two sensor failures result in runout harmonics that depend on the location of each failed sensor. This analysis only considers failure of opposing pairs of sensors because the prototype 8-sensor array is designed for this failure configuration to reduce common-mode noise and provide better thermal stability. The effect of opposing sensor pair failure and other two-sensor failure geometries can be predicted using (8). To study the effect of failed sensor pairs that lie along a measurement axis, simulation results are shown in Table 2.6 for sensors 1 and 5 failed using the 8-sensor array. These two sensors lie along the x1 measurement axis in the 8-sensor array. The increase in runout and measurement error caused by failure of an additional on-axis sensor can be seen by comparison of these results to single sensor 1 failure shown previously in Table 2.1.

Table 2.6 Harmonic amplitudes for 8-sensor array, sensors 1 & 5 failed

		j=1		j=2	
k	γ_k^{NF}	**simulation**	γ_{1k}^{F}	**simulation**	γ_{2k}^{F}
1	1.0	0.4999	0.5000	0.9998	1.000
2	0	0.0000	0.0000	0.0000	0.000
3	0	0.5003	0.5000	0.0000	0.000
4	0	0.0000	0.0000	0.0000	0.000
5	0	0.5003	0.5000	0.0000	0.000
6	0	0.0000	0.0000	0.0000	0.000
7	1.0	0.4995	0.5000	0.9990	1.000

This simulation shows good agreement with harmonic magnitude predictions for each measurement axis. The x1 sensor signal contains significant runout and measurement error for odd harmonics but completely eliminates even harmonics. If synchronous amplitude was adjusted using an expression similar to (10), the x1 sensor signal would act like an unfailed 4-sensor array. The x2 sensor signal is unaffected by this failure configuration because both $T_{2,1}$ and $T_{2,5}$ entries in the 8-sensor WGM are zero. Similar results are obtained for opposing sensor pair failure along the x2 direction, where even harmonics are eliminated in the x2 sensor signal and the x1 sensor signal is unaffected. These results support the generalized findings from single sensor failure analysis for on-axis sensor failures.

According to single sensor failure results for off-axis failures, loss of an opposing pair of sensors that do not lie directly on a measurement axis should alter both sensor array output signals. To show this effect, simulation results for failure of sensor 2 and sensor 6 in the 8-sensor array are shown with predicted harmonic amplitudes in Table 2.7. Since these two sensors are located at equal angles from the two perpendicular measurement directions, failure of this off-axis pair should produce equal attenuation of signal harmonics in each array output signal. Additional runout and measurement error caused by failure of the opposing off-axis sensor can be seen by comparison to single sensor 2 failure shown previously in Table 2.2.

Table 2.7 Harmonic amplitudes for 8-sensor array, sensors 2 & 6 failed

		j=1		j=2	
k	γ_k^{NF}	**simulation**	γ_{1k}^{F}	**simulation**	γ_{2k}^{F}
1	1.0	0.7904	0.6464	0.7904	0.646
2	0	0.0000	0.0000	0.0000	0.000
3	0	0.3537	0.3536	0.3537	0.354
4	0	0.0000	0.0000	0.0000	0.000
5	0	0.3537	0.3536	0.3537	0.354
6	0	0.0000	0.0000	0.0000	0.000
7	1.0	0.7898	0.6464	0.7898	0.646

This simulation shows less runout and measurement error for off-axis sensor pair failure as compared to failed sensor pairs that lie directly on a measurement axis. While only one array output signal is affected by loss of an on-axis sensor pair, both array output signals are affected by off-axis sensor pair failure. For both opposing sensor pair failure scenarios, even harmonics are eliminated in sensor array outputs as predicted using (8). However, simulation results show that synchronous measurement error is less than expected and runout error for the 7^{th} harmonic is greater than expected. This suggests that synchronous amplitude cannot be accurately predicted and adjusted to correct measurement error after failure of two opposing sensors.

The results from single sensor failures in the 16-sensor array showed that the effect of off-axis sensor failure is related to the location of the failed sensor. To extend these results to failure of opposing sensor pairs, simulation results for failure of sensor 2 and sensor 10 of the 16-sensor array are shown in Table 2.8. This sensor pair is located nearer the x1 measurement axis and can be expected to affect the x1 array output signal to a greater degree. The change in runout and measurement error caused by failure of the opposing sensor in this larger array can be seen by comparison to single sensor 2 failure in the 16-sensor array shown previously in Table 2.3.

Table 2.8 Harmonic amplitudes for 16-sensor array, sensors 2 & 10 failed

		j=1		j=2	
k	γ_k^{NF}	**simulation**	γ_{1k}^{F}	**simulation**	γ_{2k}^{F}
1	1.0	0.7911	0.7690	0.9668	0.904
2	0	0.0000	0.0000	0.0000	0.000
3	0	0.2310	0.2310	0.0957	0.096
4	0	0.0000	0.0000	0.0000	0.000
5	0	0.2312	0.2310	0.0958	0.096
6	0	0.0000	0.0000	0.0000	0.000
7	0	0.2307	0.2310	0.0955	0.096
8	0	0.0000	0.0000	0.0000	0.000
9	0	0.2308	0.2310	0.0956	0.096
10	0	0.0000	0.0000	0.0000	0.000
11	0	0.2316	0.2310	0.0959	0.096
12	0	0.0000	0.0000	0.0000	0.000
13	0	0.2312	0.2310	0.0958	0.096
14	0	0.0000	0.0000	0.0000	0.000
15	1.0	0.7902	0.7690	0.9658	0.904

These results also show complete elimination of even runout harmonics for each array output signal. Runout error in the remaining odd harmonics is lower for sensor pair failure when the total number of sensors is increased. Simulation results for intermediate runout harmonics agree well with prediction, but synchronous amplitude and the magnitude of the 15^{th} harmonic still do not match.

Loss of more than two sensors from the 8-sensor array was shown by Li to result in array failure even when using the SIA. Since the approach used here does not update the WGM for different failure scenarios, additional sensor failures are not studied. This failure analysis shows that runout and measurement error can be predicted using (9) for single sensor failures. In addition, synchronous measurement error can be reduced for single failures by applying an amplitude adjustment factor when allowable tolerances are exceeded. In general, sensor failure effects can be classified by their effect on array outputs according to their location with respect to each measurement axis.

2.4 DESIGN OF SENSOR ARRAY PROTOTYPE

Although simulation results show that the sensor array can successfully remove selected runout harmonics in certain failure cases, testing on a real system is required for verification. While many simplifying assumptions were made during simulation, signal accuracy on the real system depends on many factors that can degrade signal quality. These detrimental effects can be attributed to various sources that must be identified before proceeding with system design. In this way, the sensor array can be designed to optimize signal quality throughout the design process. This approach offers greater flexibility than do design modifications once problems are identified in later design stages. The effects of circuit design parameters, rotor speed, and environmental noise are discussed.

To evaluate performance improvements of the sensor array, a common commercial position transducer system is used for comparison. The sensor selected is the *3300 XL 8mm Proximity Transducer System* manufactured by Bently-Nevada [19]. This system consists of one eddy-current proximity probe, one shielded extension cable, and one *Proximitor* Sensor. The sensor array uses the same probes and extension cables as the commercial system, but the *Proximitor* Sensor is replaced with a different circuit. The new circuit is responsible for generation of the carrier signal, demodulation of the return signal, and processing of all individual sensor voltages into a single array output signal for each control direction. In this way, improvements in signal processing can be measured rather than differences in probe or cable construction. Design objectives are to meet or exceed performance of the commercial system while providing a signal similar in magnitude and linearity. This requirement allows integration of the new sensor array into existing control systems.

Design of the new oscillator-demodulator circuit requires an understanding of the operating principles behind eddy current transducers [20]. These sensors measure gap distance without rotor contact by sensing changes in complex impedance with target motion. Each probe emits a high frequency magnetic field from an internal coil that induces eddy currents in the target material. These eddy currents set up an opposing

magnetic field that reduces the inductance of the primary circuit in proportion to target distance. A typical sensor circuit can be modeled as an air-gap transformer with the secondary coil shorted within the target material. This model can be conveniently represented by a variable resistor and inductor in series.

As the air-gap between the coil and target is varied, the inductance and resistance of the equivalent circuit changes. The accuracy and thermal stability of the oscillator circuit depend on the quality factor, Q calculated as

$$Q = \frac{\omega L(x)}{R(x)} \tag{12}$$

where ω is the sensor excitation frequency. Attractive sensors have a high quality factor that can be achieved by large inductance, small resistance, and high frequency excitation. Inductance of the coil changes with air gap for target distances less than the coil radius, limiting maximum sensing range to this dimension. The choice of excitation frequency depends on many competing factors explained in the following discussion.

The probe cable and interwinding capacitance causes internal resonance of the oscillator circuit at the self-resonant frequency (SRF). When the circuit is excited at its SRF, gain increases in a manner similar to a single degree of freedom mechanical oscillator. The SRF changes with target distance as a result of variations in coil inductance according to

$$SRF = \frac{1}{2\pi\sqrt{LC_{total}}} \tag{13}$$

where the total capacitance includes contributions from the cable and coil windings. Excitation frequency is selected at least a factor of 3 below the SRF and coincides with a separate resonant frequency caused by a parallel capacitor to maximize amplitude of the carrier signal. At this excitation frequency, changes in the SRF with gap distance result in variations in signal amplitude. The amplitude modulated carrier signal is demodulated by an envelope detection circuit to produce a voltage corresponding to target offset. Changes in this output voltage with gap distance are described by sensor sensitivity. Attractive sensors have linear sensitivity for a useful operating range,

commonly 10 to 90 mils. This linear range and the magnitude of sensor sensitivity are determined by many factors including maximum coil inductance, parallel capacitance, and excitation frequency and amplitude.

Rotor speed can also greatly affect sensor array output amplitude due to bandwidth limitations. For each sensor, target motion in the sensing direction is synchronous with rotor speed. As rotor spin speed increases, the frequency of rotor vibration may exceed the bandwidth of the sensing system. This causes attenuation in measured vibration amplitude and could lead to poor controller performance. To prevent this problem, the bandwidth of the sensor array drive circuit should be greater than the maximum frequency encountered in operation. Typical bandwidth of a commercial eddy current oscillator-demodulator circuit is on the order of 10 kHz [19].

Other than sensor runout disturbance, undesirable signal components are introduced into the feedback loop by environmental noise. Sources of environmental noise include electromagnetic interference from magnetic bearing power amplifiers, sensor crosstalk, imperfect components and adjacent wiring. While many of these noise sources are not addressed in this thesis, other researchers have studied them in depth. Jansen et. al. [21] provide a thorough analysis on the effects of PWM switching frequency and magnetic field noise near the carrier frequency. Environmental noise radiated into the probe cables can be minimized by using the same shielded cables as commercial systems. These environmental disturbances can be effectively reduced by proper circuit design.

A common problem encountered when using multiple eddy-current probes in close proximity is caused by mutual interference known as crosstalk. This phenomenon results from interaction of the magnetic fields induced by adjacent probes. When the rotor is displaced these magnetic fields load the oscillation circuit of each probe, slightly altering the frequency of the carrier signal. When adjacent probes are loaded unequally, the difference in their carrier frequencies causes beat modulation of each signal known as sensor crosstalk. This interference can be particularly troublesome in a sensor array such as the one described in this thesis. As the number of sensors in the array increases,

the distance between sensors is reduced and the effect of the induced magnetic fields on adjacent probes becomes more pronounced. Thus, a means to combat sensor crosstalk must be designed into the system. Dever et. al. [22] addressed this problem by preloading adjacent sensors using capacitors. This provided enough difference in carrier frequency to significantly reduce crosstalk effects in the control band. However, utilization of a single oscillation circuit for all sensors in an array allows for a very simple solution to crosstalk problems. By using a single carrier signal to drive all sensors in the array, any change in carrier signal frequency is shared by all probes and no frequency difference exists. This common carrier frequency eliminates sensor crosstalk effects for all sensors in the 8-sensor array drive circuit and can also be used to remove common-mode noise.

The prototype circuit is simplified by taking advantage of WGM anti-symmetry for opposing sensor gains. By driving opposing sensors exactly 180° out of phase using the same carrier wave, voltage signals from opposing sensor pairs can be summed to create a difference signal. After demodulation, the $n/2$ difference signals are amplified according to the WGM and then summed to produce array output signals corresponding to rotor displacements. Additional circuitry is added to bias each output voltage to zero at the nominal gap distance. The differential signal approach results in lower circuit cost, better thermal stability and reduced common-mode noise. However, fault tolerance to single sensor failures is lost.

When a single sensor fails, the difference signal approaches the unfailed voltage signal from its opposing counterpart. This voltage signal is very large in comparison to the original difference signal and dominates sensor array output. To maintain usable sensor array outputs using this differential approach, single sensor failure requires that the opposing sensor also be removed to drive the difference to zero. For this reason, the prototype sensor array drive circuit described here is not tolerant of single sensor failures. This prototype is designed to verify sensor array operation for the unfailed case only, with sensor failure effects analyzed by theory and simulation as shown previously.

Consideration of these effects allows construction of an oscillator-demodulator circuit that provides a useful rotor position signal while minimizing signal-to-noise ratio. The prototype circuit allows verification of sensor array performance when all sensors are operational. Variable components are used in the prototype to allow adjustments during the design stage. Potentiometers are used to vary op-amp gains for WGM implementation. Variable parallel capacitors allow adjustment of the internal resonance frequency to optimize individual sensor sensitivity and linearity. Although these components allow flexibility during initial design, slight differences in capacitance and individual amplifier gains result in different sensitivity for each axis and less than ideal attenuation of runout harmonics as shown by testing results.

Future revisions of the sensor array demodulation circuit should allow independent failure of individual probes. This modification would sacrifice the benefits of simplified construction, reduced thermal effects and lower noise amplitudes for fault tolerance to sensor failures. These revisions include separate amplification and voltage biasing of individual sensor signals to allow single sensor failures and to avoid DC shifts as determined by simulation results. However, the current prototype circuit can be tested to characterize performance for the unfailed case. Performance characteristics for the unfailed 8-sensor array prototype as built are described in the following section.

2.5 TESTING OF SENSOR ARRAY PROTOTYPE

To verify theoretical performance capabilities of the unfailed 8-sensor array, several tests are conducted on the prototype system. These tests are intended to quantify the runout reduction achieved by the sensor array and to confirm the performance limits identified previously. Testing requires additional hardware designed to evaluate sensor performance in a controlled environment. Two different fixtures are used to quantify sensor performance for both rotating and non-rotating rotors. These fixtures require two different rotors to simulate low and high runout amplitude conditions.

A device with the ability to adjust gap distance is used during construction of the sensor drive circuit. This positioning fixture is used to measure sensor sensitivity, linear

range and noise levels for a non-rotating shaft. Since this fixture is used for gap adjustment with a stationary shaft, the target rotor does not introduce any significant levels of runout. Precision adjustment of shaft position within the sensor array is accomplished using a dual-axis micrometer stage. This stage is attached to the lower of two parallel plates separated by lock-nuts on threaded columns. The circular probe array is mounted to a cylindrical aluminum shell attached to the upper plate. To set nominal gap distances and center the steel shaft, an acetal sleeve is inserted into the aluminum shell. The outer diameter of the sleeve is used to adjust the probe gaps while the internal diameter of this sleeve allows a sliding fit over the shaft when centered. Actual shaft motion is measured mechanically using dial indicators on each axis. The positioning fixture is shown in Figure 2.6.

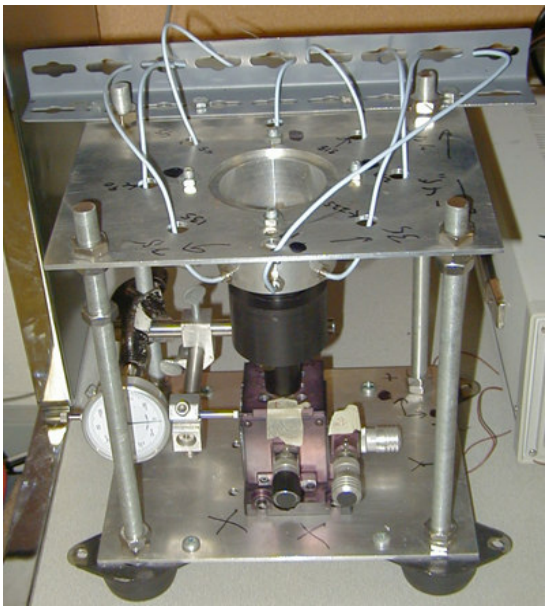

Figure 2.6 Positioning fixture used for stationary gap measurements

To experimentally evaluate bandwidth and runout reduction capabilities of the sensor array, a rotor with a known runout pattern is used as the target in a rotating test fixture. This fixture uses precision ball bearings rather than magnetic bearings to support the rotor. The ball bearings are mounted on O-rings inside an aluminum housing

that contains the 8-sensor array. This housing is rigidly attached to a plate that slides into a large steel containment vessel for safety reasons. Rotor speed is controlled by a small AC motor coupled to the shaft using a short rigid spline so that torsional vibrations can be neglected. Gap distances for each probe are set by tightening locknuts at the proper location using a calibration fixture with precision steel shims. The rotating test fixture is shown in Figure 2.7.

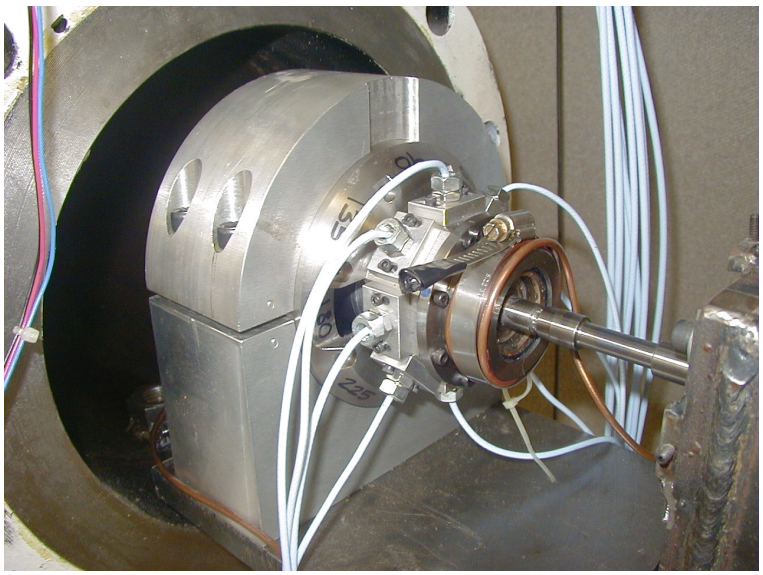

Figure 2.7 Rotating test fixture used for runout evaluation

To compare actual disturbance rejection to theoretical performance, a runout pattern similar to that used for numerical simulation is created on the target rotor. The amplitude of each harmonic is adjusted to obtain a smooth signal with a nearly-zero mean value to simplify machining. This signal is then summed with a circular profile to generate a curve that represents the target rotor outer diameter. Using CNC machine tools, this pattern can be reproduced on the target rotor with sufficient accuracy. The desired experimental runout signal generated using MATLAB is shown with the measured profile of the machined rotor in Figure 2.8. Comparisons to theoretical performance use this modified runout signal rather than the equal amplitude harmonic

signal used for numerical simulation alone. Harmonic amplitudes of the desired runout pattern are shown in Figure 2.9, though it should be noted that actual total runout differs slightly from this intended signal due to uncontrolled electronic runout and limitations of the machining process.

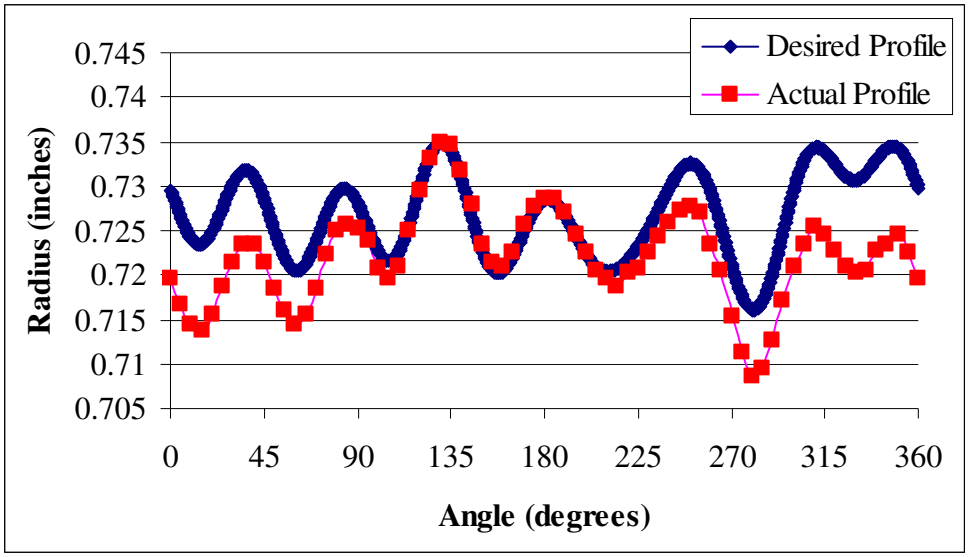

Figure 2.8 Runout signal used to evaluate reduction of harmonic amplitudes

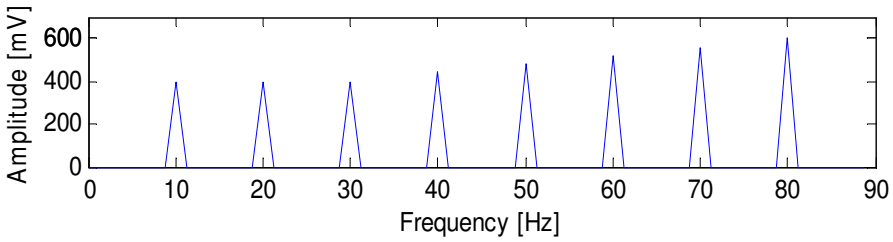

Figure 2.9 Fourier amplitudes of modified runout signal

Additional equipment used for testing of the prototype sensor array include 1 function generator, 2 power supplies, 1 digital oscilloscope and 1 dynamic signal analyzer. The function generator supplies a 6.7 Volt, 1.09 MHz sine wave to the drive circuit to create the carrier signal as described in the design section. The power supplies deliver ± 15 VDC to the drive circuit. Rotor speed is measured using the oscilloscope

connected to a once-per-revolution hall probe signal used for motor control. Outputs of the sensor array are monitored using the dynamic signal analyzer in both the time and frequency domains. Runout reduction is evaluated by the frequency spectrum for the unfailed case in the following section.

2.6 TESTING RESULTS

The two different test fixtures used to evaluate sensor array performance assess different design objectives. These objectives require that the sensor array meet or exceed performance of commercially available individual eddy-current proximity transducers. Performance metrics are identified as sensitivity, linearity, noise amplitude and runout reduction. Sensitivity, linear range and noise levels are measured using the positioning fixture shown in Figure 2.6. Runout reduction is evaluated using the rotating test fixture shown in Figure 2.7. All tests on the sensor array consider the unfailed state only. Testing methods and results are described here for evaluation of the 8-sensor array prototype and the commercial transducer system.

Sensitivity and linearity of the 8-sensor array prototype are determined by moving the target in small increments using the positioning device. Actual displacements are measured with dial indicators and compared to sensor outputs. This test is performed for motion along each axis with both the sensor array and commercial systems. Sensitivity for each test is determined by the slope of a best-fit line obtained from the data points using linear regression. Linearity is evaluated by the coefficient of determination (R^2) value for each regression analysis. Test range is limited by the micrometer stage to [-20, 35] mils on the x1-axis and [-35, 35] mils on the x2-axis. Data for the sensor array prototype is shown for each axis with best-fit trendlines in Figures 2.10 and 2.11.

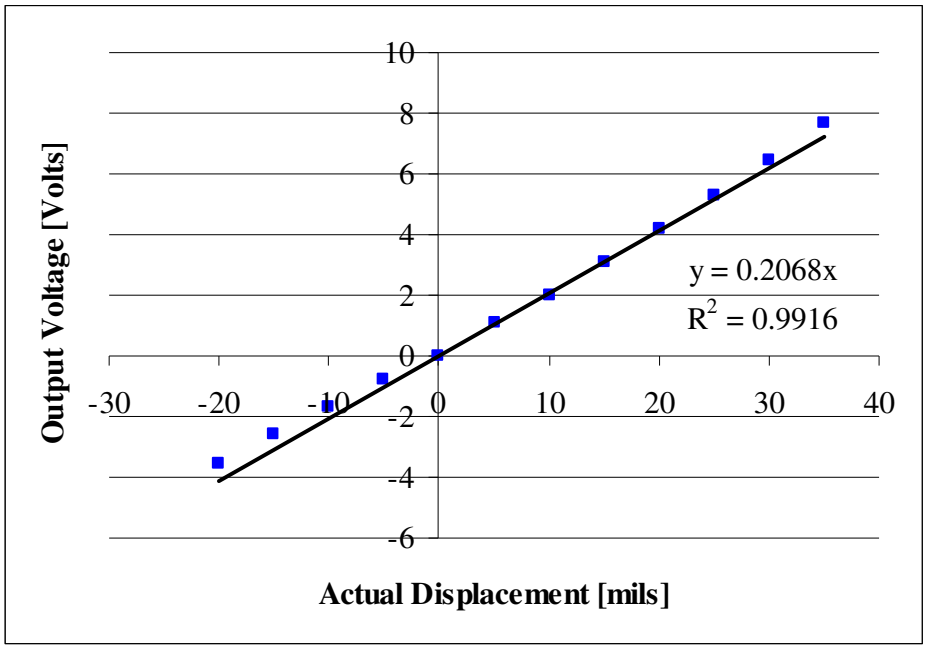

Figure 2.10 Sensor array voltage vs position for x1-axis

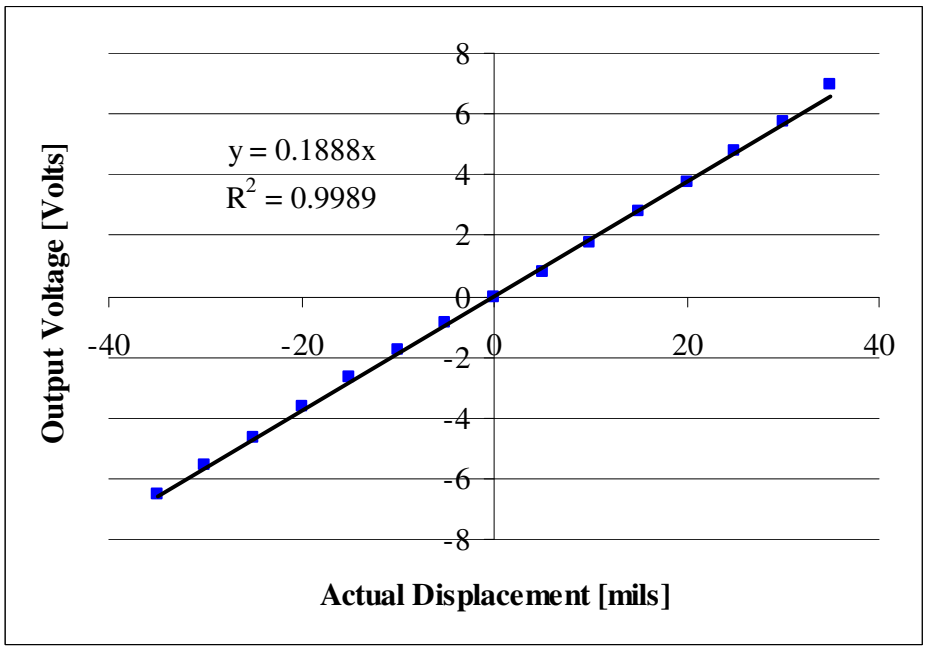

Figure 2.11 Sensor array voltage vs position for x2-axis

Sensor array sensitivity is not the same for each axis as shown by the slope of the best-fit trendline. This difference can be attributed the variable potentiometers and capacitors used for construction of the drive circuit. In theory, if all components are equal-valued and excited using the same signal then sensitivity is the same for each axis. This speculation is not validated in this thesis since it would require construction of a new drive circuit for the sensor array. However, this test shows that the prototype sensor array can match the $200\,{}^{mV}/_{mil}$ sensitivity of commercial sensor systems on each axis independently. Future testing should be performed to verify symmetric sensitivity of an array that uses more stable electronic components.

Linearity of the relationship between voltage and target offset is required so that rotor displacement can be easily determined from the sensor signal without using look-up tables or complex operations. These tests show acceptable linearity in the test range with approximate equivalent displacement errors of 0.5 mil along the x1-axis and 0.1 mil along the x2-axis. In comparison, identical testing on the commercial system yielded an R^2 value of 0.9999, corresponding to approximately 0.01 mil displacement error. Deviations of sensor array voltage from the linear trendline become more pronounced near the limits of the test range. To properly validate linearity within reasonable operating limits of the sensor array, a precision positioning stage with greater range should be employed. Additional experiments on the array drive circuitry should also examine linearity at different excitation frequencies or parallel capacitance values.

Noise levels are evaluated for a stationary shaft centered in the 8-sensor array prototype. In this test, no magnetic actuators are present so that noise can be attributed solely to component imperfections and interference radiated into the cables and wiring. Broadband noise is evaluated by its maximum amplitude for the two array outputs measured on the x1-x2 plane using a digital oscilloscope. Noise levels for the sensor array are compared to the Bently Nevada *Proximitor* transducer system using 2 orthogonal probes targeting the same shaft. The sampled data from the digital oscilloscope for both sensor systems are shown in Figure 2.12.

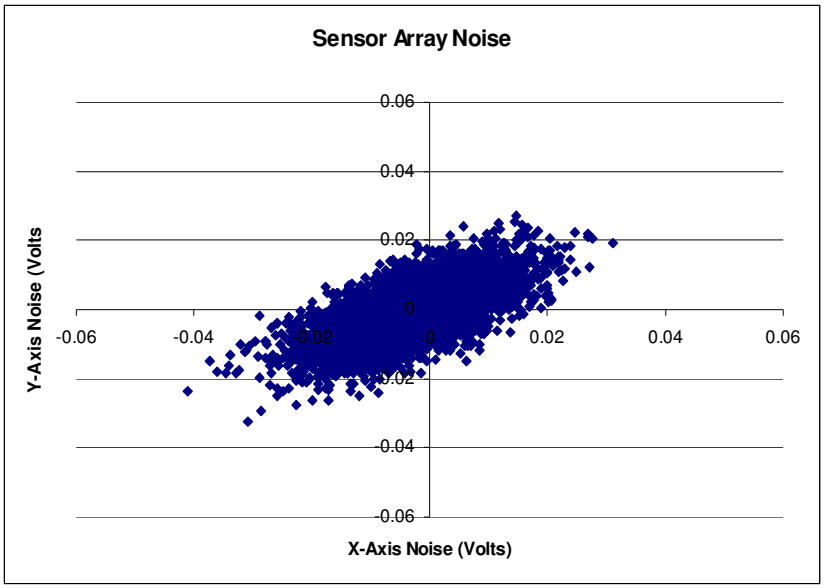

(a)

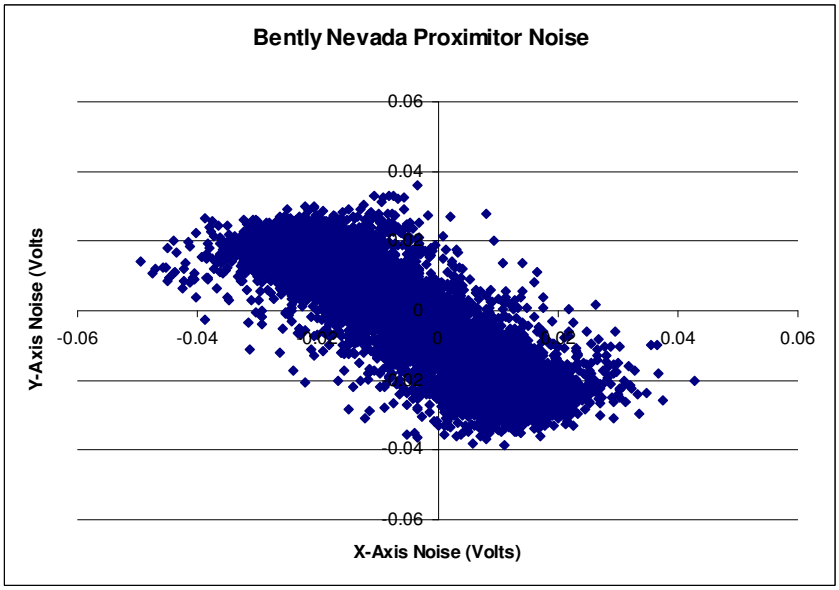

(b)

Figure 2.12 Broadband noise amplitude for 8-sensor array (a) and Bently Nevada *Proximitor* (b)

Noise data for the stationary shaft shows that the 8-sensor array prototype introduces less broadband noise into the sensor signal that the commercial system used for comparison. This is expected since the prototype drive circuit used the differential

approach to reduce common-mode noise. It is also interesting to note the phase relationships between x1 and x2 noise signals for each sensor system. While the commercial system signals are out of phase, the sensor array noise signals are in phase. Since all probes in the sensor array use a common carrier signal, noise disturbances in array outputs will always be in phase. The phase relationship for the commercial system may be arbitrary since carrier signals are generated independently. Approximate maximum noise amplitudes for both x1 and x2 signals are listed for the sensor array and the commercial system in Table 2.9. Displacement uncertainty resulting from sensor noise is shown assuming ideal sensor sensitivity of 200 $^{mV}/_{mil}$ on each axis.

Table 2.9 Noise amplitudes for sensor array prototype and commercial system

	Signal Noise (V_{pp})	**Equivalent Uncertainty**
Sensor Array x1-axis	30 mV	0.15 mil
Sensor Array x2-axis	20 mV	0.10 mil
Proximitor x1-axis	35 mV	0.18 mil
Proximitor x2-axis	35 mV	0.18 mil

The above tests are intended to verify basic functionality of the sensor array for position measurement of a non-rotating shaft. Improvements in runout reduction for the unfailed 8-sensor array can only be shown by testing on a rotating shaft with a known runout profile. Performance of the 8-sensor array is evaluated by runout and measurement error for the unfailed case using the rotating test fixture. Testing is performed first using a single commercial sensor to confirm testing methods and equipment and to measure the actual total runout harmonics present in the test rotor. A frequency spectrum of the single sensor measurement with the machined test runout pattern is shown in Figure 2.13. This frequency spectrum shows the instantaneous amplitudes of rotor vibration and runout harmonics for a rotational frequency of 55 Hz.

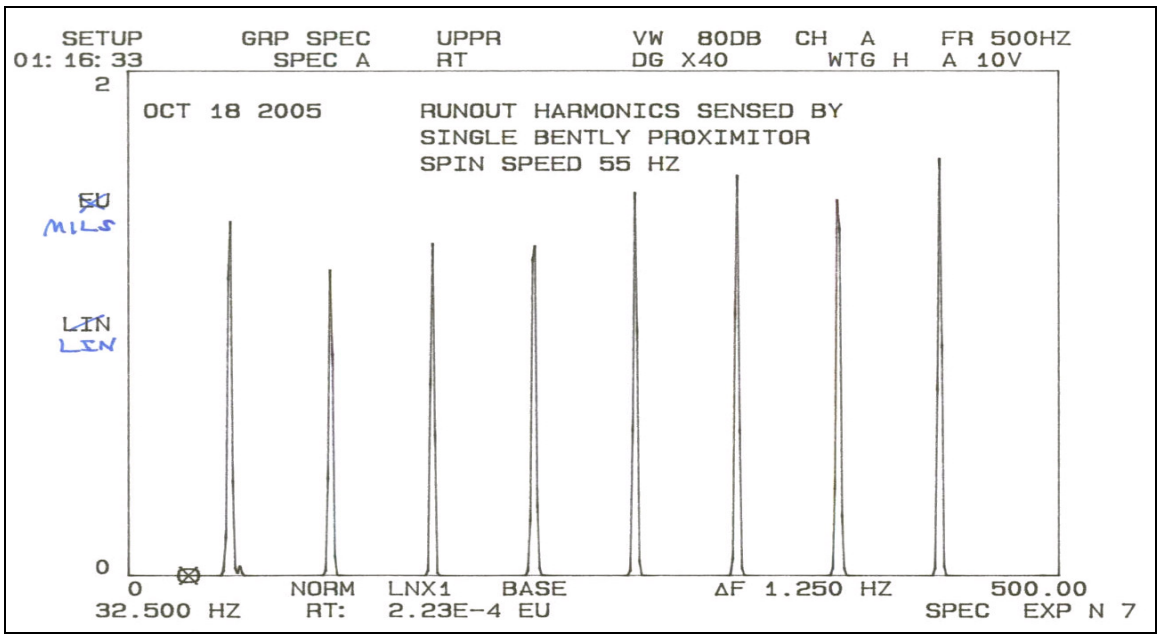

Figure 2.13 Frequency spectrum of vibration and runout measured by a single sensor

Harmonic amplitudes shown in this frequency spectrum do not exactly match the intended runout profile due to machining errors and electronic runout. Despite these differences, this signal can be used to effectively determine sensor array runout reduction.

According to theory and numerical simulation, the unfailed 8-sensor array should completely remove runout harmonics $k = 2$ to $k = 6$ while preserving the synchronous signal component. Runout reduction for the 8-sensor array is measured by the amplitudes of runout harmonics relative to single sensor runout. Assuming the single sensor accurately detects rotor vibration, synchronous measurement error in the prototype sensor array is the ratio of the $k = 1$ array output harmonic to single sensor data. While complete attenuation of runout harmonics is not expected for the real system, significant reduction is achieved. Harmonic amplitudes are shown for a single sensor and the sensor array in Table 2.10, where γ_k^T represents runout and measurement error from testing. To effectively compare sensor array output harmonics to single sensor measurements, amplitudes are averaged to account for transient variations.

Table 2.10 Harmonic amplitudes measured using a single sensor (Actual) and 8-sensor array (Measured) with runout and measurement error

k	γ_k^{NF}	Actual amplitude (mV)	Measured amplitude (mV)	$\overline{\gamma_k^T}$
1	1.0	277	282.0	1.0181
2	0	270	17.6	0.0652
3	0	248	34.6	0.1395
4	0	312	20.7	0.0663
5	0	298	37.0	0.1242
6	0	323	11.9	0.0368
7	1.0	325	272.0	0.8369

These results show that the prototype 8-sensor array with no sensor failures can significantly reduce runout errors as predicted by theory and simulations. Synchronous amplitude is only slightly altered by the sensor array, although small deviations from single sensor measurements can be caused by differences in actual rotor vibration. Runout harmonics are reduced unequally due to the adjustable components used in the prototype drive circuit. A frequency spectrum of the x1 array output in Figure 2.14 shows how the 8-sensor array reduces the effect of sensor runout as compared to the frequency spectrum in Figure 2.13. The x2 array output contains signal harmonics similar to the x1 sensor array signal

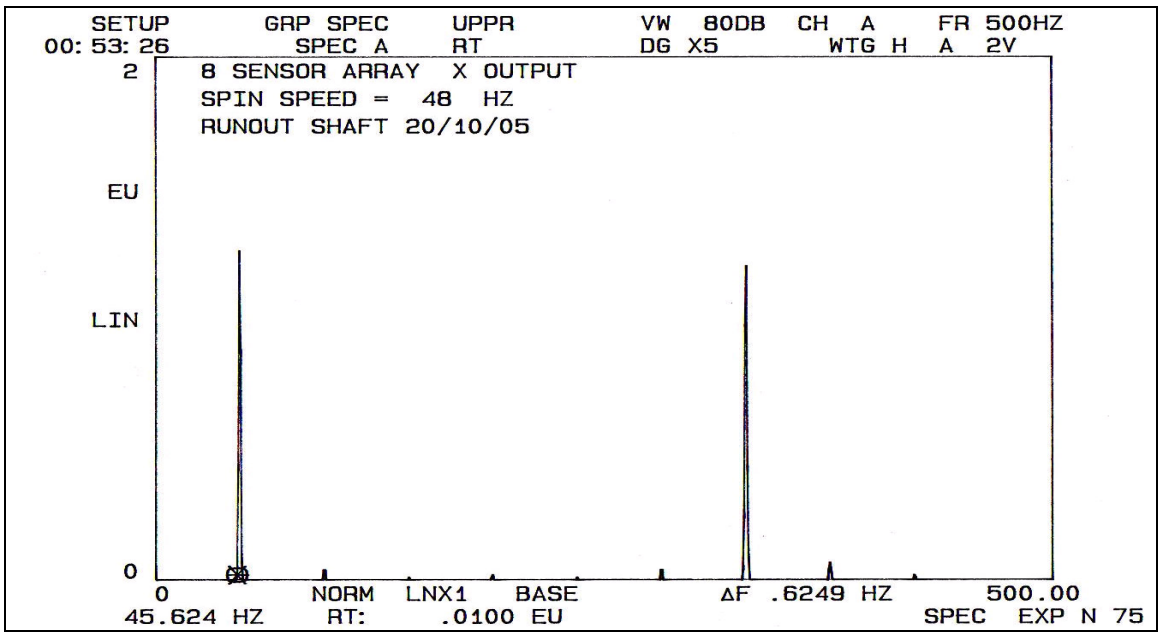

Figure 2.14 Frequency spectrum of test rotor runout measured by 8-sensor array

While the runout reduction test is performed at relatively low rotor speeds, it is useful to know the maximum frequency that can be accurately measured by the sensor array. This maximum frequency is defined as bandwidth of the sensor array, but is difficult to measure experimentally. Direct measurement of 2dB signal amplitude attenuation at high speeds would require a perfectly balanced shaft with a known runout pattern. If this were possible, synchronous signal amplitude could be attributed entirely to runout which is largely independent of speed. Real rotors always have some imbalance that results in speed-dependent vibration. As a result, the relationship between vibration amplitude and sensor limitations cannot be distinguished without a true measurement of instantaneous shaft position during operation. Since design requirements only stipulate that the sensor array meet performance of commercial systems, measured vibration amplitude at higher speeds can be evaluated relative to the commercial system. This is accomplished by peak-hold signal analysis of the sensor array and commercial sensor signals for rotor speeds from 0 to 5 kHz. The peak-hold frequency spectrums of the two sensor systems are shown in Figure 2.15.

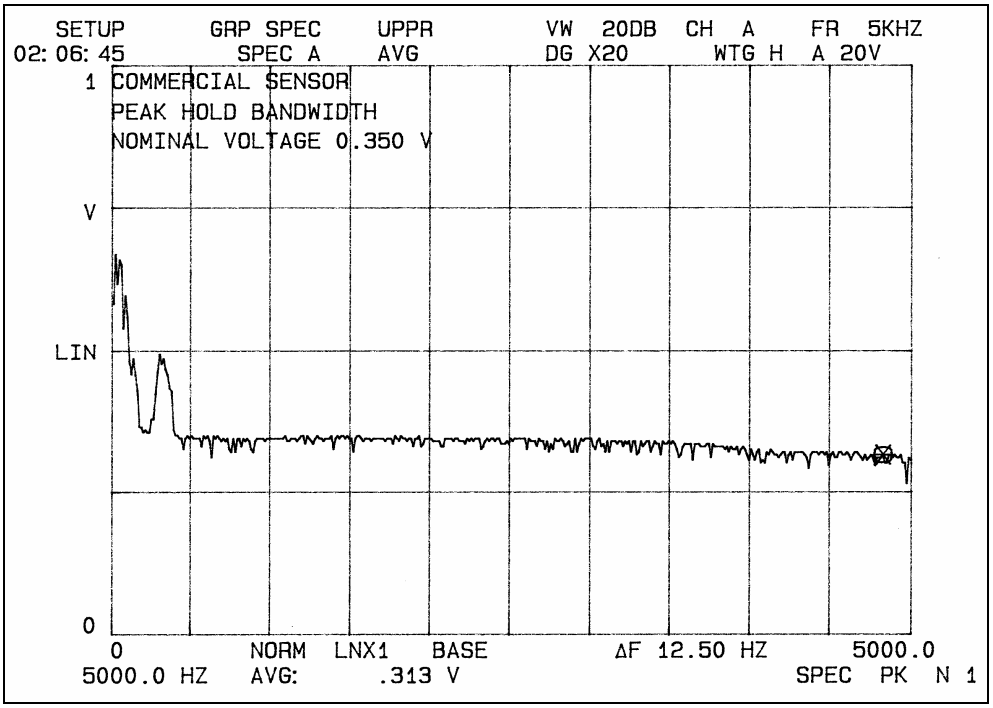

(a)

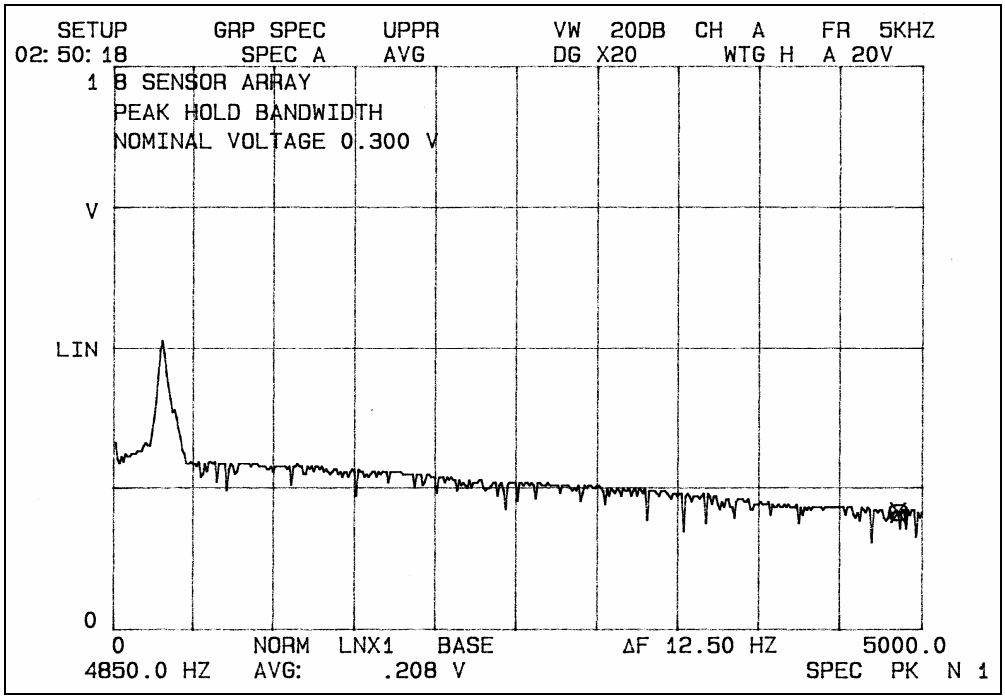

(b)

Figure 2.15 Peak-hold frequency spectrum of commercial sensor (a) and 8-sensor array prototype (b)

Comparison of the peak-hold frequency spectrums obtained using each sensor system reveal some interesting results. Both sensors recorded a resonant peak near 300 Hz, but the commercial sensor measured additional low frequency vibrations. Since the bandwidth test requires slow speed variation, it is possible that these low frequency signals are the result of rotor speed changes in the time record. Another possibility is that the sensor array removes subharmonic in addition to superharmonic signal components. This latter possibility is investigated using (8) and is not possible according to present theory.

The peak-hold frequency spectrums also show a difference between measured amplitudes after resonance for each sensor. This difference results from the greater amplitude of higher harmonics in the sample runout pattern. Since the sensor array significantly reduces these harmonics, they do not contribute to recorded peak amplitudes. Thus, the peak-hold frequency spectrum of the commercial sensor is actually a measurement of one of these higher harmonics rather than the synchronous signal. However, comparison of signal trends with increasing speed can still be used to indirectly evaluate bandwidth of the prototype sensor array. Assuming that the steady drop in peak-hold amplitude of the sensor array is not caused by a reduction in synchronous vibration, the bandwidth of the sensor array is estimated at around 4.8 kHz.

Testing on the prototype 8-sensor array supports theory and simulation results for runout reduction with no sensor failures. Sensitivity and linearity tests on the positioning fixture confirm compatibility of the sensor array with existing magnetic bearing control systems. Total measurement errors due to environmental noise and deviations from the linear correlation with gap distance do not exceed 1 mil across the sensing range. These results show that the circular sensor array is an effective method of monitoring rotor position.

2.7 SUMMARY AND FUTURE WORK

This research shows that the circular sensor array can effectively remove certain harmonics of runout from the rotor position signal. This is proven using analytical expressions that describe the magnitude of each runout harmonic and supported using numerical simulations and testing of a prototype system for the unfailed case. Performance of the sensor array is affected by sensor failures when using the NSIA by an increase in sensor runout and measurement error. When measurement error exceeds allowable tolerances, synchronous amplitude can be corrected for single sensor failures using an amplitude adjustment factor. This adjustment significantly reduces measurement error with a slight increase in runout. Simulations of two sensor failures for opposing sensor pairs show complete elimination of even runout harmonics. Sensor failure analysis shows that failure effects on each sensor array output are related to the angular location of the failed sensors. This is shown for on-axis and off-axis sensor failures for the 8-sensor and 16-sensor arrays.

Further research should be performed on the sensor array before integration in a magnetic bearing control loop. Symmetric sensitivity for each measurement direction should be achieved through construction using stable electronic components. Phase lag caused by signal processing should be evaluated and compared to commercial systems. The revised drive circuit should be altered as described to allow single sensor failures. For these single failure cases, measurements of harmonic amplitudes should be made to test synchronous amplitude adjustment factors. In addition, the effect of fluctuating magnetic field interference should be examined. After successful completion of these tests, the NSIA sensor array may be utilized in a magnetic bearing control system with confidence in its ability to supply an accurate position signal with reduced runout even in the presence of single sensor failures.

CHAPTER III

NONLINEAR ANALYSIS OF HOMOPOLAR MAGNETIC BEARINGS

3.1 INTRODUCTION

Active magnetic bearings (AMBs) are inherently nonlinear dynamic systems due to the quadratic relationship between magnetic force and control current. This nonlinearity results in behavior that cannot be explained by linear vibration theory such as orbital equilibrium state sensitivity to initial conditions and bifurcation behavior resulting in jump phenomena and subharmonic steady state response. Nonlinear system response can often be approximated using an assumption of small motions about an equilibrium state. This characteristic allows linear control of the AMB system through bias linearization, where bias flux is supplied either by permanent magnets or a biasing current. As rotor motions become larger, nonlinearities begin to dominate magnetic bearing control forces. This chapter analyzes such nonlinearities in homopolar magnetic bearings using numerical techniques to simulate a simplified rotor-bearing system. Frequency response curves for the nonlinear magnetic bearing are compared to a similar linearized bearing model to illustrate the effect of the nonlinear terms and unusual rotor oscillations near nonlinear resonance are analyzed to characterize bifurcation behavior.

Many different techniques have been developed to study the behavior of non-autonomous nonlinear systems. Analytical methods such as harmonic balance, trigonometric collocation, Floquet theory and multiple scales provide useful insight into the stability and bifurcation behavior of orbital equilibrium states and their domains of attraction. These methods require a deterministic relationship between control currents and magnetic control forces. Numerical methods such as shooting or direct numerical integration can be used to understand nonlinear behavior when analytical techniques cannot be applied. While current numerical techniques are not as powerful as analytical methods, they can be used to determine locally stable and unstable periodic orbital equilibrium states, generate frequency response curves, and locate and characterize

various bifurcations. While nonlinearities in heteropolar magnetic bearings have been studied using analytical tools, nonlinear analysis of homopolar magnetic bearings requires the use of numerical methods due to complex flux path equations that decouple control currents and magnetic flux at each pole.

Homopolar magnetic bearings provide several advantages over traditional heteropolar configurations. In heteropolar bearings, opposing magnetic poles are arranged in a single plane around the rotor circumference. This arrangement causes magnetic flux to continuously alternate direction into and out of the rotor. Each time the flux path reverses direction, energy is lost due to hysteresis. This reversal causes increased control effort and results in inductive heating of the rotor. Homopolar magnetic bearings reduce these effects by arranging opposing poles in two parallel planes separated axially along the rotor. While parasitic losses are reduced in homopolar bearings, magnetic flux paths become more complicated functions of all air gap reluctances. Rotor displacements from magnetic center reduce reluctance of air gaps in the displacement direction, resulting in an increase of corresponding magnetic flux. Magnetic forces at each pole are proportional to the square of magnetic flux, giving rise to the nonlinear effects under analysis. Although the AMB controller stabilizes both magnetic pole configurations by directing current to poles away from rotor deflection, analysis of the homopolar bearing requires modeling these complex flux paths through the rotor. This model necessitates simultaneous solution of n independent magnetic circuit equations for an n-pole homopolar bearing, excluding many analytical methods for nonlinear study.

In this thesis, magnetic flux equations are solved by linear matrix algebra within a fourth-order Runge-Kutta numerical integration routine. Governing equations for the homopolar magnetic bearing are developed in the following section for the nonlinear and linearized systems. These equations are numerically integrated using strict tolerances to obtain accurate results for small rotor motions. Stable nonlinear response to a periodic unbalance force is investigated and compared to the linearized system using frequency response curves. From these stable frequency response plots, locally unstable orbital

equilibrium states are determined by the shooting method. As a byproduct of shooting, eigenvalues of a numeric monodromy matrix are used to characterize bifurcations as rotor speed is varied. These frequency-dependent bifurcations are shown to progress toward quasiperiodic behavior classified by the periodicity of steady state response as shown using Poincaré maps. These tools allow better understanding of nonlinear response in homopolar magnetic bearings and illustrate deviations from linear model predictions. Results obtained from this study can be used to select desirable magnetic bearing operating conditions for higher rotor speeds and safer operation.

3.2 SYSTEM MODEL

This thesis uses a simplified model of a single homopolar radial AMB for nonlinear analysis. In this model, only cylindrical rigid body motion is considered so that shaft rotations about axes perpendicular to the spin axis and resulting rotordynamic effects are neglected. Torsional vibrations are also not considered in this analysis since magnetic bearings do not directly control rotor torques. The homopolar magnetic bearing provides magnetic bias flux using permanent magnets and control flux using 6 identical poles equally spaced around the rotor. Control currents are computed using a PD controller and an idealized current distribution matrix where inductance effects are neglected. The rigid rotor is modeled as a lumped mass with two degrees of freedom, X and Y as shown in Figure 3.1. Instantaneous rotor position along these axes is measured by ideal proximity probes biased to zero at the magnetic center. The homopolar magnetic bearing is assumed to be perfectly constructed so that the magnetic center is coincident with the geometric center.

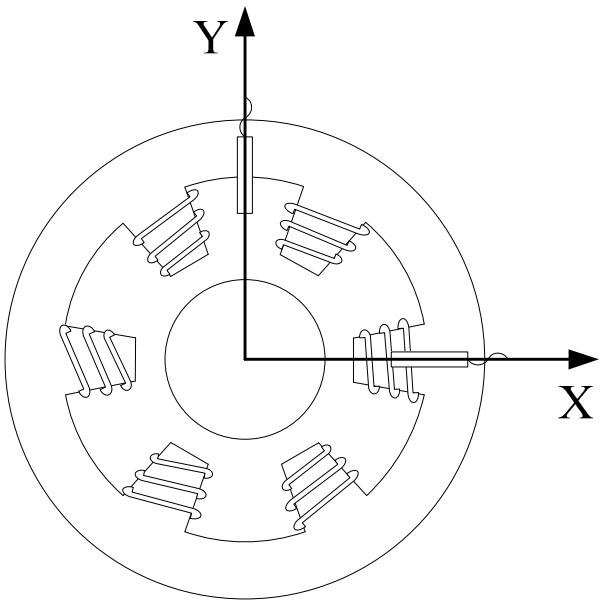

Figure 3.1 Rigid rotor-bearing model used for analysis

Forces acting on the rigid rotor consist of control forces from the magnetic actuators and periodic inertial forces from unbalance vibration. Rotor weight due to gravity is neglected in this analysis. These forces are assumed to act entirely in directions that can be described by the two rotor degrees of freedom. Magnetic forces are determined by solving a set of magnetic circuit equations for magnetic flux using control voltages supplied by a proportional-derivative (PD) controller. Unbalance vibration results from an assumed eccentricity between the center of mass and the center of rotation. This eccentricity is varied to magnify nonlinear response characteristics, but is independent of rotor speed for each analysis. Assumed mass properties used for this analysis are shown in Table 3.1.

Table 3.1 Mass properties of model rotor-bearing system

Property	Value	Units
Mass of rotor	20	kg
Eccentricity	2.5	mils
Clearance	20	mils

The governing equations of motion for this rotor supported by a homopolar magnetic bearing result from Newton's third law for each degree of freedom as

$$\begin{aligned} m\ddot{x} &= me\omega^2 \cos(\omega t) - F_{m,x} \\ m\ddot{y} &= me\omega^2 \sin(\omega t) - F_{m,y} \end{aligned} \tag{14}$$

where $F_{m,j}$ represents the magnetic force acting on the rotor in the j[th] control direction. This magnetic force is calculated using both the nonlinear bearing model and the linearized bearing model. Derivation of the magnetic force term for each model is shown in the following sections.

NONLINEAR MODEL

The radial magnetic bearing is modeled using an equivalent magnetic circuit for the flux path through the control coils, air gaps and rotor cross-section. This analysis considers a 6-pole homopolar radial magnetic bearing biased using permanent magnets. Magnetic flux acting on the rotor consists of both bias flux supplied by the permanent magnets and control flux supplied by the 6 control coils. For the development of governing equations, all permanent magnets are lumped into a single source element with internal reluctance. It is assumed that the rotor, coils and wiring have negligible reluctance so that all magnetic flux is contained in the permanent magnets and air gaps between poles and the rotor surface. Core loss due to eddy currents, flux saturation, and hysteresis and other secondary effects are neglected. The equivalent magnetic circuit for this model is shown in Figure 3.2 with assumed flux directions.

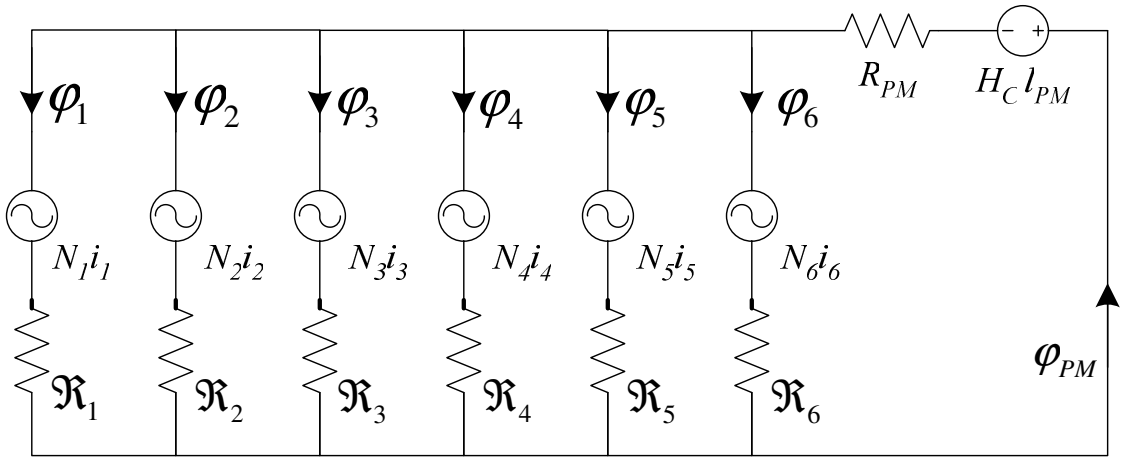

Figure 3.2 Magnetic circuit used to solve for coil currents and magnetic field strength

Application of Ampere's Law to each loop in the magnetic circuit results in a set of 6 coupled differential equations for magnetic fluxes and coil currents. Assuming uniform magnetic fields within each air gap and negligible fringing and leakage effects, these differential equations become one-dimensional linear algebraic equations that relate coil currents to gap fluxes. One additional independent equation needed to eliminate permanent magnet flux is found using flux conservation. The resulting set of coupled linear equations is

$$\begin{bmatrix} \Re_1 & -\Re_2 & 0 & 0 & 0 & 0 \\ 0 & \Re_2 & -\Re_3 & 0 & 0 & 0 \\ 0 & 0 & \Re_3 & -\Re_4 & 0 & 0 \\ 0 & 0 & 0 & \Re_4 & -\Re_5 & 0 \\ 0 & 0 & 0 & 0 & \Re_5 & -\Re_6 \\ 0 & 0 & 0 & 0 & 0 & \Re_6 \end{bmatrix} \begin{bmatrix} \Phi_1 \\ \Phi_2 \\ \Phi_3 \\ \Phi_4 \\ \Phi_5 \\ \Phi_6 \end{bmatrix} = \begin{bmatrix} N_1 & -N_2 & 0 & 0 & 0 & 0 \\ 0 & N_2 & -N_3 & 0 & 0 & 0 \\ 0 & 0 & N_3 & -N_4 & 0 & 0 \\ 0 & 0 & 0 & N_4 & -N_5 & 0 \\ 0 & 0 & 0 & 0 & N_5 & -N_6 \\ 0 & 0 & 0 & 0 & 0 & N_6 \end{bmatrix} \begin{bmatrix} i_1 \\ i_2 \\ i_3 \\ i_4 \\ i_5 \\ i_6 \end{bmatrix} + \begin{bmatrix} 0 \\ 0 \\ 0 \\ 0 \\ 0 \\ -H_{PM}\, l_{PM} \end{bmatrix} \tag{15}$$

where $\Re_i$ describes the reluctance of the ith pole air gap defined as

$$\Re_i = \frac{d_i}{\mu_0 A_{pole}} \tag{16}$$

and d_i represents the length of the ith air gap. In analogy to Ohm's law, these equations can be arranged in matrix form as

$$R\Phi = N\,i + H \tag{17}$$

where the right hand side represents total magnetic field strength supplied by both permanent magnets (Ni) and electromagnetic coils (H) in opposing directions. In general, magnetic field strength is related to flux density by the definition

$$B = \mu H \tag{18}$$

where μ represents magnetic permeability of the medium, usually air. Flux density is related to magnetic flux by

$$B = \frac{\varphi}{A} \tag{19}$$

Along with Ampere's Law, these equations form the foundation from which all other governing equations are derived. This approach has been used in analysis of many other electromagnetic systems with similar results [10,18].

In the presence of a non-zero external magnetic control field, permanent magnetic flux is reduced as described by the second quadrant of the magnetization hysteresis loop known as the demagnetization curve. This curve represents the normal operating range of many electromagnetic devices that use permanent magnets acting against an externally applied magnetic field. In magnetic bearings, the external magnetic field is supplied by the control coils with a direction opposite the flux path of the permanent magnet. The demagnetization curve shows how flux density from the permanent magnet is reduced by this external control field and can be approximated by a linear relationship between external magnetic field strength (H_{ext}) and permanent magnetic flux density (B_{PM}) as shown in Figure 3.3.

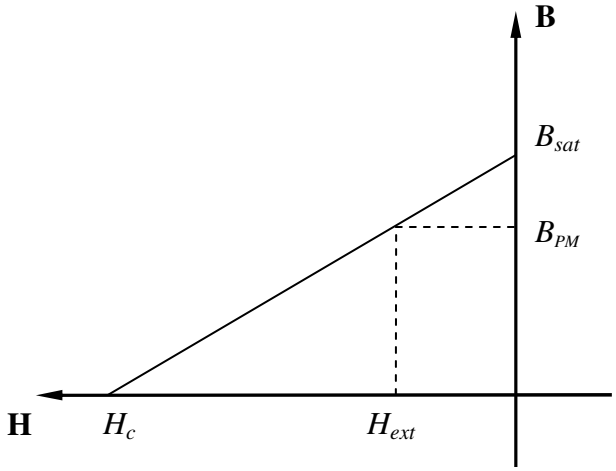

Figure 3.3 Permanent magnet demagnetization curve

The points at which this line intersects each axis are performance characteristics of permanent magnets known as remanence and coercivity. Remanence (B_{sat}) is the flux density supplied by the permanent magnet when no external demagnetizing force is present. Coercivity (H_C) describes the strength of an external demagnetizing field required to reduce permanent magnetic flux to zero. The slope of the line connecting these two points is equal to the permanent magnet permeability (μ_{PM}), which is close to the permeability of air. Using this linear relationship, the reduced flux density from the permanent magnet can be approximated as

$$B_{PM} = B_{sat} - \mu_{PM} H_{ext} \tag{20}$$

Dividing by μ_{PM}, and substituting (18,19) for the external magnetic field strength,

$$H_{PM} = H_C - \frac{\phi_{PM}}{\mu_{PM} A_{PM}} \tag{21}$$

This expression is substituted into the matrix H in (15) and the second term is moved to the left-hand side of the magnetic circuit flux equation. Using flux conservation, this term can be treated as permanent magnet reluctance shown by

$$\Re_{PM} = \frac{l_{PM}}{\mu_{PM} A_{PM}} \tag{22}$$

Replacing the unknown permanent magnetic field strength in (15) with the flux-dependent terms derived from the demagnetization curve results in the complete magnetic circuit equations

$$\begin{bmatrix} \Re_1 & -\Re_2 & 0 & 0 & 0 & 0 \\ 0 & \Re_2 & -\Re_3 & 0 & 0 & 0 \\ 0 & 0 & \Re_3 & -\Re_4 & 0 & 0 \\ 0 & 0 & 0 & \Re_4 & -\Re_5 & 0 \\ 0 & 0 & 0 & 0 & \Re_5 & -\Re_6 \\ \Re_{PM} & \Re_{PM} & \Re_{PM} & \Re_{PM} & \Re_{PM} & \Re_{PM}+\Re_6 \end{bmatrix} \begin{bmatrix} \Phi_1 \\ \Phi_2 \\ \Phi_3 \\ \Phi_4 \\ \Phi_5 \\ \Phi_6 \end{bmatrix} = \begin{bmatrix} N_1 & -N_2 & 0 & 0 & 0 & 0 \\ 0 & N_2 & -N_3 & 0 & 0 & 0 \\ 0 & 0 & N_3 & -N_4 & 0 & 0 \\ 0 & 0 & 0 & N_4 & -N_5 & 0 \\ 0 & 0 & 0 & 0 & N_5 & -N_6 \\ 0 & 0 & 0 & 0 & 0 & N_6 \end{bmatrix} \begin{bmatrix} i_1 \\ i_2 \\ i_3 \\ i_4 \\ i_5 \\ i_6 \end{bmatrix} + \begin{bmatrix} 0 \\ 0 \\ 0 \\ 0 \\ 0 \\ -H_C l_{PM} \end{bmatrix} \tag{23}$$

These equations allow computation of the total magnetic flux at the rotor surface for each air gap. Air gap fluxes are used to determine the magnetic control force contribution from each pole as a function of coil currents.

Magnetic air gap fluxes for each pole location can be calculated from (23) by premultiplication of the inverse reluctance matrix. These gap fluxes are the summation of control flux from the electromagnetic coils and demagnetized bias flux from the permanent magnets, represented by the terms

$$\begin{aligned} \Phi_{control} &= R^{-1} N\, i \\ \Phi_{bias} &= R^{-1} H \end{aligned} \tag{24}$$

Control flux is dictated by control currents from the position feedback controller described below. Using the demagnetized form of the magnetic circuit equations, bias flux can be considered constant. The assumptions of zero flux leakage and fringing effects simplify analysis of magnetic bearing operation, but are not accurate in practice. Leakage results from flux circulation between poles of the permanent magnets, while fringing describes nonparallel flux paths within the air gaps. To model these effects, permanent magnet bias flux is de-rated according to a leakage factor and total magnetic flux is de-rated to account for fringing. These factors are derived from detailed 3-D

finite element models [10] and are given in Table 3.2 with other magnetic properties of the homopolar bearing used for this analysis.

Table 3.2 Properties of magnetic bearing poles and permanent magnets used in analysis

Property	Value	Units
Area of one pole face	4.750E-04	m^2
Area of PM cross-section	2.563E-03	m^2
Length of all PMs	1.011E-02	m
Coercivity of PMs	9.500E+05	A m^{-1}
Permeability of air	4π E-07	---
Relative permeability of PM	1.055	---
Number of turns on each coil	24	---
Leakage Factor	0.596	---
Fringing Factor	0.900	---

Coil currents are generated by two independent control voltages determined by separate PD controllers for each axis using feedback position signals. In practice, instantaneous rotor position is measured by eddy current transducers and rotor velocity is found from these measurements by numerical differentiation. For the present simulations of rotor motion, rotor position and velocity at finite time steps are determined by numerical integration of the second order governing equations of motion in (14). Sensor runout and other sources of measurement noise are not considered in this analysis of nonlinear effects. Voltage from these ideal sensors is biased to zero when the shaft is perfectly centered and increases linearly with a sensitivity of 200 mV/mil as gap length is increased.

Control voltages for each axis are passed through a 2-by-6 current distribution matrix (CDM) designed for fault tolerance capability before entering the power amplifiers. In this model, power amplifier gains are included in the CDM. The resulting CDM used in this analysis for a 6-pole homopolar radial bearing with no pole failures is

$$CDM = \begin{bmatrix} 1.539 & 0 \\ 0.7695 & 1.335 \\ -0.7695 & 1.335 \\ -1.539 & 0 \\ -0.7695 & -1.335 \\ 0.7695 & -1.335 \end{bmatrix} \tag{25}$$

This matrix maps two independent control voltage signals into 6 separate currents that pass through the electromagnetic control coils. Actual magnetic bearings require a decoupling choke to remove singularities in the inductance matrix. This analysis assumes ideal power amplifiers so that inductance effects can be neglected.

Using this control strategy, rotor position is sensed and fed back the controller, where control voltages for each axis are computed using PD control gains. These two control voltages are distributed to each pole using the CDM. Power amplifiers for each pole pass the appropriate current through the coils to generate electromagnetic control forces. This approach is illustrated by the block diagram in Figure 3.4.

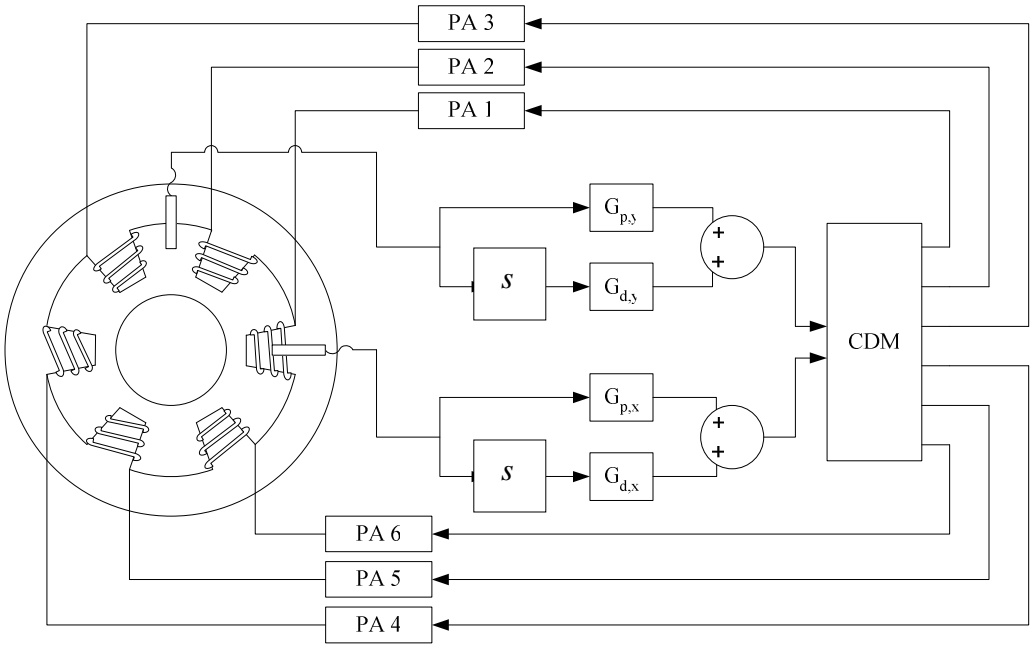

Figure 3.4 Control strategy used in the homopolar magnetic bearing

Nonlinear behavior in this magnetic bearing model results from nonlinearities in the magnetic forces used to support the rotor. The magnitude of each magnetic pole force is related to the i^{th} pole magnetic flux by the one-dimensional Maxwell stress tensor

$$F_i = \frac{\Phi_i^2}{2\mu_0 A_{pole}} \tag{26}$$

This quadratic relationship between magnetomotive force and magnetic flux produces the nonlinear characteristics of magnetic bearings. The magnetic force contribution from each pole to the magnetic force acting on the rotor in each control direction is a function of pole location. Total magnetic force in the horizontal (x) and vertical (y) directions for the nonlinear model is given by

$$\begin{aligned} F_{m,x} &= \sum_{i=1}^{6} F_i \cos(\theta_i) \\ F_{m,y} &= \sum_{i=1}^{6} F_i \sin(\theta_i) \end{aligned} \tag{27}$$

where θ_i indicates the angle between each pole and the positive x-axis. These nonlinear magnetic force terms are substituted into (14) to determine nonlinear rotor response.

Additional assumptions are utilized in this analysis for model simplification. Sensor dynamics accounting for runout, bandwidth and phase lag are not modeled. Also, in practice the rotor must be coupled to some device to impart or extract rotational energy. Torsional effects and drag caused by this coupling are not considered. The required magnetic support forces and speeds in this model are assumed low enough that flux saturation and slew rate limitations can be neglected. Curvature of pole faces and the rotor surface and small amounts of rotational damping present in the real system due to air drag, eddy currents and other effects are also neglected in this analysis. Despite such simplifying assumptions, these equations provide a good indication of nonlinear effects in homopolar magnetic bearings.

LINEAR MODEL

Linearization of magnetic forces in homopolar magnetic bearings is commonly employed to allow linear control of the nonlinear system. This process requires bias flux supplied by permanent magnets or biasing currents to allow a Taylor series expansion of magnetomotive force about the equilibrium point at magnetic center. Bias linearization of magnetic forces yields an accurate approximation of nonlinear magnetic forces for small control inputs. As rotor displacements approach the bearing clearance, nonlinear magnetic forces diverge from the linearized prediction. This process has been extensively described by other researchers [11] and is not repeated here. Using bias linearization, magnetic forces can be approximated as

$$F_{m,x} = k_p x + k_v V_x \tag{28}$$

where the terms k_p and k_v represent the position stiffness and voltage stiffness of the magnetic bearing, respectively. In heteropolar bearings, the values of these stiffnesses can be derived analytically. For homopolar bearings, these values must be determined experimentally. In this analysis, position stiffness and voltage stiffness are determined using numerical simulations of the full nonlinear system.

The two stiffness terms of the linearized magnetic force equation result from separation of the two different magnetic flux sources in permanent magnet biased magnetic bearings. Position stiffness is the ratio of magnetic force to lateral displacement of a non-rotating shaft when the feedback control gains are identically zero. In this state, magnetic forces acting on the rotor surface are the result of bias flux from the permanent magnets alone. Voltage stiffness is the ratio of magnetic force to control voltage for a non-rotating shaft fixed at the bearing center. Magnetic forces for this measurement result from the combined contribution of bias flux and control flux for a constant gap distance. Simulations of the full nonlinear magnetic bearing model are conducted with the appropriate constraints to determine the values of position stiffness and voltage stiffness as shown in Figures 3.5 and 3.6, respectively.

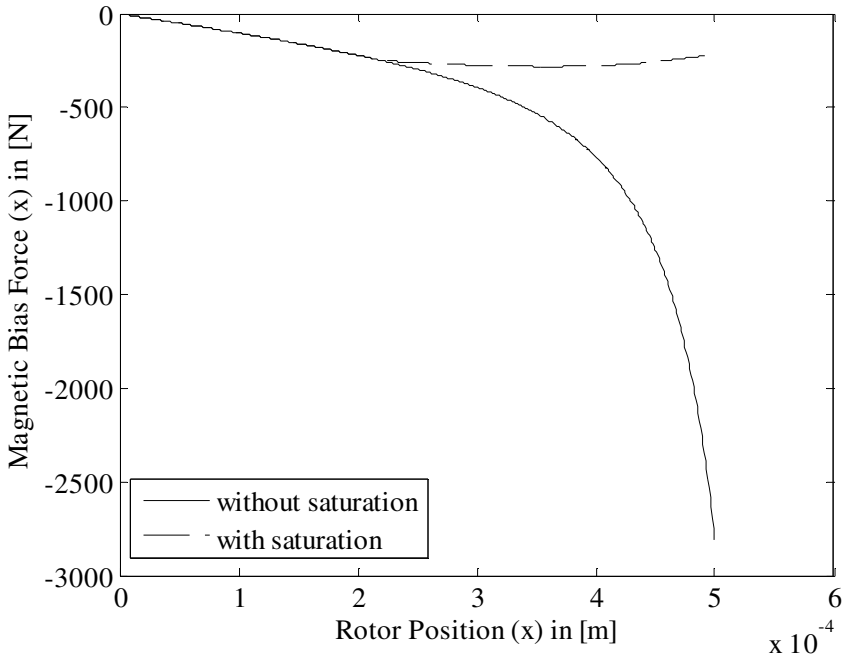

Figure 3.5 Nonlinear magnetic force vs rotor position for linearized position stiffness

For the simplified bearing model considered in this research, the relationship between magnetic force and rotor position with no feedback control is linear for small rotor motions and becomes nonlinear as rotor deflection approaches the bearing clearance. If the effects of flux saturation are considered, magnetic force cannot exceed a limiting value as shown by the dashed line in Figure 3.5. For small rotor motions below 0.2 mm in this case, flux saturation effects do not alter steady state rotor oscillations. Position stiffness is found by the ratio of magnetic force to displacement in the linear range close to the bearing center. For the magnetic bearing parameters in Table 3.2, position stiffness is measured as -751.3 $^{N}/_{mm}$ from simulation results. Since magnetic force increases as the rotor is displaced in the positive direction, position stiffness from the permanent magnets alone results in a destabilizing force. This negative stiffness causes an unstable equilibrium point at the bearing center. The rotor is stabilized by adding feedback control that can be approximated by the linear voltage stiffness term.

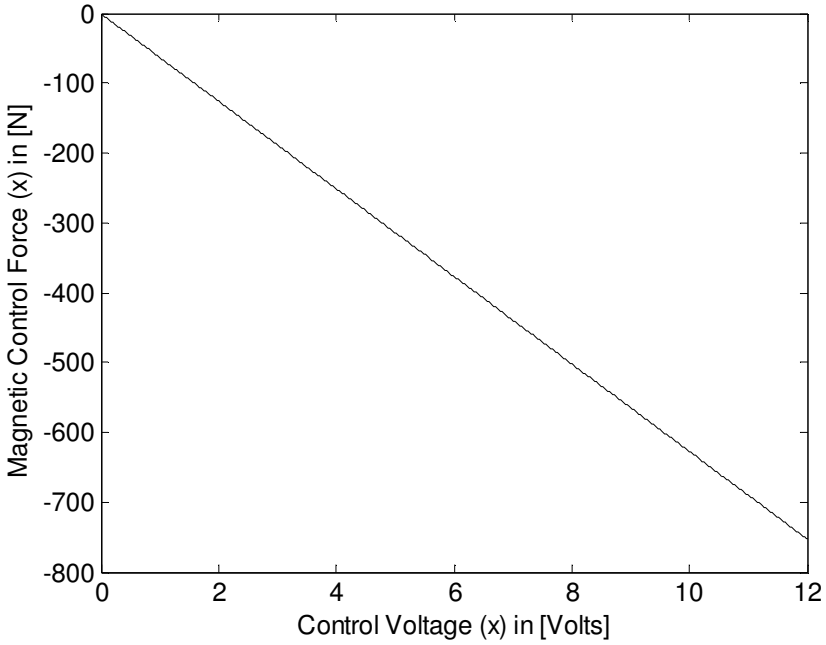

Figure 3.6 Nonlinear magnetic force vs control voltage for linearized voltage stiffness

By fixing all gap lengths with the rotor centered, bias flux from the permanent magnets is constant and total magnetic force increases linearly with control voltage as shown in Figure 3.6. The simplified bearing model studied here does not deviate from the model that includes flux saturation for the voltage range considered. For the magnetic bearing parameters used in this analysis, voltage stiffness is measured as +54.15 $^{N}/_{V}$ from these simulation results. Voltage stiffness results in a positive restoring force that stabilizes the rotor about a stable equilibrium point at the bearing center. Once the values of voltage and position stiffness are known, the linearized magnetic force term can be substituted into (14) to determine transient rotor response by direct numerical integration.

The linearized governing equations for the homopolar magnetic bearing describe a linear, time invariant (LTI) system characterized by special relationships between excitation force input and rotor response. After transient solution components have died out, response of LTI systems is synchronous with excitation frequency at a different amplitude and shift in phase. In such systems, only one solution exists whose stability is

independent of excitation input. Steady state amplitude of this stable solution can easily be determined using an assumed solution approach known as complex variable analysis. This method takes advantage of LTI system properties and the simplicity of exponential function derivatives by using complex exponentials to represent the periodic steady state solution as

$$x(t) = \tilde{X}\, e^{i\omega t} \tag{29}$$

where the variable $\tilde{X}$ is a complex number. Complex variable analysis of LTI systems requires that the governing equations be expressed only in terms of this assumed solution and its derivatives. Expanding the linearized magnetic force equation using a PD controller for the control voltage yields

$$F_{m,x} = k_p x + k_v (G_p \xi x + G_d \xi \dot{x}) \tag{30}$$

where ξ represents the sensor sensitivity. This representation of magnetic control force is substituted into the governing equations of motion to give

$$\begin{aligned} \ddot{x} + k_{v,x} G_{d,x} \xi \dot{x} + (k_{p,x} + k_{v,x} G_{p,x} \xi) x &= me\omega^2 \cos(\omega t) \\ \ddot{y} + k_{v,y} G_{d,y} \xi \dot{y} + (k_{p,y} + k_{v,y} G_{p,y} \xi) y &= me\omega^2 \sin(\omega t) \end{aligned} \tag{31}$$

Substituting the assumed solution and its derivatives into the governing equation of motion gives

$$\tilde{X}(-m\omega^2 + k_p + k_v G_p \xi + i\omega k_v G_d \omega)\, e^{i\omega t} = \mathrm{Re}(\tilde{F}\, e^{i\omega t}) \tag{32}$$

Solving (32) for $\tilde{X}$ and taking the magnitude of the complex result yields an expression for the steady state amplitude of periodic vibrations about the rotor static equilibrium position,

$$\left|\tilde{X}\right| = \frac{me\omega^2}{\sqrt{(k_p + k_v G_p \xi - m\omega^2)^2 + (\omega k_v G_d \xi)^2}} \tag{33}$$

This expression is plotted versus excitation frequency to obtain the frequency response characteristics of the linearized homopolar magnetic bearing. This linearized system prediction is compared to the full nonlinear system frequency response in the following section to determine the effect of the nonlinear terms.

3.3 FREQUENCY RESPONSE

Analysis of dynamic systems requires an understanding of steady state system response at different excitation frequencies. In rotordynamics, periodic excitation force caused by rotor unbalance is synchronous with rotor speed and increases in amplitude with the square of spin frequency. Linear vibrating systems respond at the same frequency as the excitation force with amplitude and phase lag that vary with excitation frequency. Nonlinear systems respond differently to periodic excitation, exhibiting resonance over a range of frequencies, sudden jumps in amplitude and subharmonic steady state response. In this section, nonlinear amplitude and phase frequency response curves for the homopolar magnetic bearing described above are compared to the frequency response curves for the linear magnetic force derived by bias linearization.

Nonlinear rotordynamic systems can possess multiple orbital equilibrium states whose local stability is influenced by the direction of changes in frequency. Stable equilibrium states may become unstable with a small change in excitation frequency, causing jumps to another stable solution. These jumps occur at different frequencies for each stable solution. For this reason, steady state amplitudes of oscillation while the rotor is accelerating may be different than amplitudes when decelerating. To fully describe frequency response of the nonlinear homopolar bearing, steady state amplitude must be determined for both increasing and decreasing rotor speeds. This requires a slowly time-varying excitation frequency expressed as

$$\omega(t) = \omega_0 + \alpha t \tag{34}$$

where the parameter α is sufficiently small to produce quasi-steady state response at a given frequency. The sign of this parameter is reversed to model rotor deceleration. In frequency response analysis, the magnitude of $\alpha = 0.0001\ {}^{rad}\!/_{s^2}$ is selected to limit transient response while ensuring reasonable computation times.

The proportional and derivative control gains applied to the feedback position signal have a significant effect on rotor-bearing frequency response. For linear systems, derivative controller gain affects the maximum amplitude of rotor vibration and the

phase reversal at resonance. Proportional controller gain affects the linearized natural frequency of rotor oscillation according to

$$\omega_{n,L} = \sqrt{\frac{k_{eff}}{m}} \tag{35}$$

where the effective stiffness for the linearized magnetic bearing is

$$k_{eff} = k_p + k_v G_p \xi \tag{36}$$

Since position stiffness is negative, it can be shown that proportional control gain must be at least

$$G_p \geq \frac{k_p}{k_v \xi} \tag{37}$$

to overcome permanent magnet bias flux and stabilize the system. This minimum value of proportional control gain is approximately $G_p = 1.76$ for the linearized stiffness terms that characterize the homopolar magnetic bearing in this analysis. With the nonlinear magnetic bearing force, variations in proportional control gain can result in very different stiffness characteristics. For small rotor displacements from static equilibrium, nonlinear bearing stiffness can be closely approximated by the linearized model. As rotor displacements become larger, nonlinear magnetic force terms result in hardening or softening spring behavior depending on the magnitude of proportional controller gain. This behavior is shown in Figure 3.7 where both linear and nonlinear magnetic forces are plotted versus rotor displacement up to the bearing clearance for various values of proportional gain.

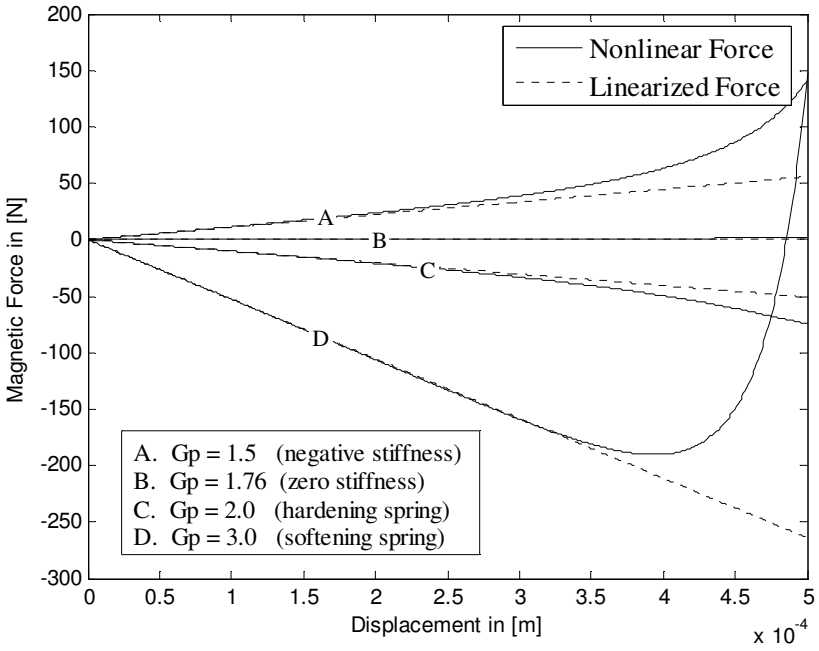

Figure 3.7 Effect of proportional control gain on magnetic bearing stiffness

This simulation shows that linearized magnetic force closely matches the nonlinear magnetic force up to approximately half the bearing clearance in this case. As predicted by linear analysis, proportional gains less than 1.76 do not provide enough control flux to stabilize rotor oscillations. For proportional control gains around 2.0, nonlinear magnetic force is greater than the linearized model prediction, resulting in hardening spring behavior near the bearing clearance. As proportional gain is increased to about 3.0, bearing stiffness decreases rapidly after diverging from the linearized force. This extreme softening spring behavior is limited in practice due to flux saturation which is not considered further in this analysis.

Both hardening and softening spring behavior result in deviations from the linear model frequency response curve such as tilting of the resonant peak, multiple orbital equilibrium states at a single frequency and sudden jumps in steady state vibration amplitude. These characteristics resemble the nonlinear behavior of the Duffing oscillator for cubic stiffness terms. As seen in Figure 3.7, nonlinearities are more

pronounced for proportional control gains that result in nonlinear softening spring stiffness. Careful selection of rotor mass properties and controller gains can limit magnetic support forces so that nonlinearities do not significantly affect rotor oscillations near resonance. However, for large or highly imbalanced rotors homopolar magnetic bearings must operate with proportional control gains in the nonlinear softening spring range. For this reason, only softening spring behavior is examined in this thesis. Rotor mass properties as shown in Table 3.1 and control gains as shown in Table 3.3 are selected to magnify nonlinear frequency response characteristics.

Table 3.3 Control gains used to analyze softening spring behavior

Proportional Control Gain	12
Derivative Control Gain	0.004

Frequency response for the nonlinear magnetic bearing force is determined by direct numerical integration at equally spaced frequency intervals for both accelerating and decelerating rotor spin speeds. Rotor acceleration is modeled using the slow time-varying excitation frequency in (34). At each frequency, integration is carried out for exactly 60 forcing cycles using a continuation method to ensure quasi-steady state response. This continuation routine uses the state values at the beginning of each forcing period to define initial conditions at the next frequency iteration to minimize transient behavior. After integrating the nonlinear governing equations at each frequency, local maxima and minima are determined by searching for sign changes in the velocity coordinates for each rotor degree of freedom. Vibration amplitude at each frequency is defined as half the maximum difference between these peaks to avoid errors caused by phase effects. The resulting frequency response curve is overlaid on the linear model complex variable prediction in Figure 3.8 for X-axis rotor vibration amplitudes. Vibration amplitudes along the Y-axis are nearly identical with slightly larger amplitudes due to pole geometry. For this reason, frequency response is not discussed separately for each axis.

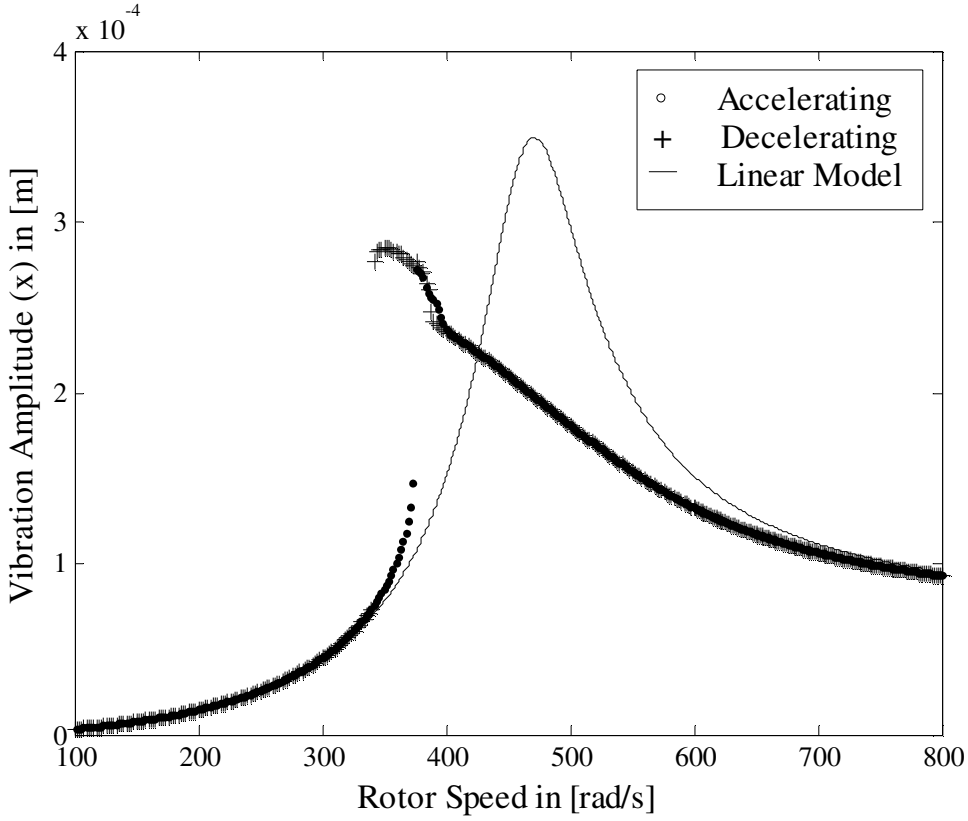

Figure 3.8 X-axis amplitude frequency response for softening spring behavior

Amplitudes of rotor oscillations show good agreement between the nonlinear and the linearized magnetic bearing model at rotor excitation frequencies away from the linearized natural frequency. Resonance behavior for the nonlinear model exhibits tilting to the left characteristic of nonlinear softening springs. At frequencies near this nonlinear resonance two stable orbital equilibrium states exist whose stability depends on the direction of rotor angular acceleration. For increasing spin speeds the stable rotor orbit experiences an upward jump at $374\ ^{rad}/_{s}$ to another stable equilibrium state. For decreasing rotor spin speeds the jump occurs at $342\ ^{rad}/_{s}$ creating a region of hysteresis in which multiple orbital equilibrium states exist at a single frequency. This behavior is also observed in the well-known Duffing oscillator which possesses a third orbital equilibrium state in this hysteresis region that is unstable for all cases. The locus of

these unstable orbital equilibrium states are determined in Section 3.4 using the shooting method. In addition to these sudden amplitude jumps, Figure 3.8 shows rotor oscillations in the hysteresis region with maximum amplitudes that do not follow the smooth trend observed elsewhere in the frequency response curve. It will be shown that rotor obits in the frequency region near nonlinear resonance experience a series of bifurcations leading to steady state oscillations containing subharmonic frequency components. This sequence is discussed in Section 3.5 using Poincaré maps and bifurcation diagrams.

As rotor speed is varied, rotor oscillations also undergo a change in phase with respect to the periodic unbalance excitation force. To estimate this phase shift, the governing equations for the homopolar magnetic bearing can be expressed in the frequency domain by taking the Laplace transform. In this way, the linearized homopolar magnetic bearing model can be expressed in the frequency domain by the transfer function

$$\frac{X(s)}{F(s)} = \frac{1}{s^2 + (k_v G_d \xi)s + (k_p + k_v G_p \xi)} \tag{38}$$

Phase frequency response of the second-order linearized magnetic bearing model is determined from this transfer function using Bode plot rules. To illustrate the phase relationship between excitation input and rotor response using the nonlinear magnetic bearing force, an algorithm similar to that used to generate the amplitude frequency response curve is employed. By choosing the number of integration time steps to result in a constant number of samples per forcing cycle, the beginning of each forcing period is exactly known. For each degree of freedom, local maxima in rotor orbits are located by searching for sign changes in the velocity when position coordinates are positive. After a sufficient number of cycles to ensure steady state behavior, phase lag at each frequency can be approximated by the number of time steps between local maxima and the beginning of each forcing period. Dividing this difference by the number of samples per forcing cycle and multiplying the result by 360° provides a reasonable approximation of nonlinear phase lag at each frequency. The approximate nonlinear

phase angle is shown with the linearized transfer function approximation in Figure 3.9 as a function of excitation frequency for increasing and decreasing spin speeds.

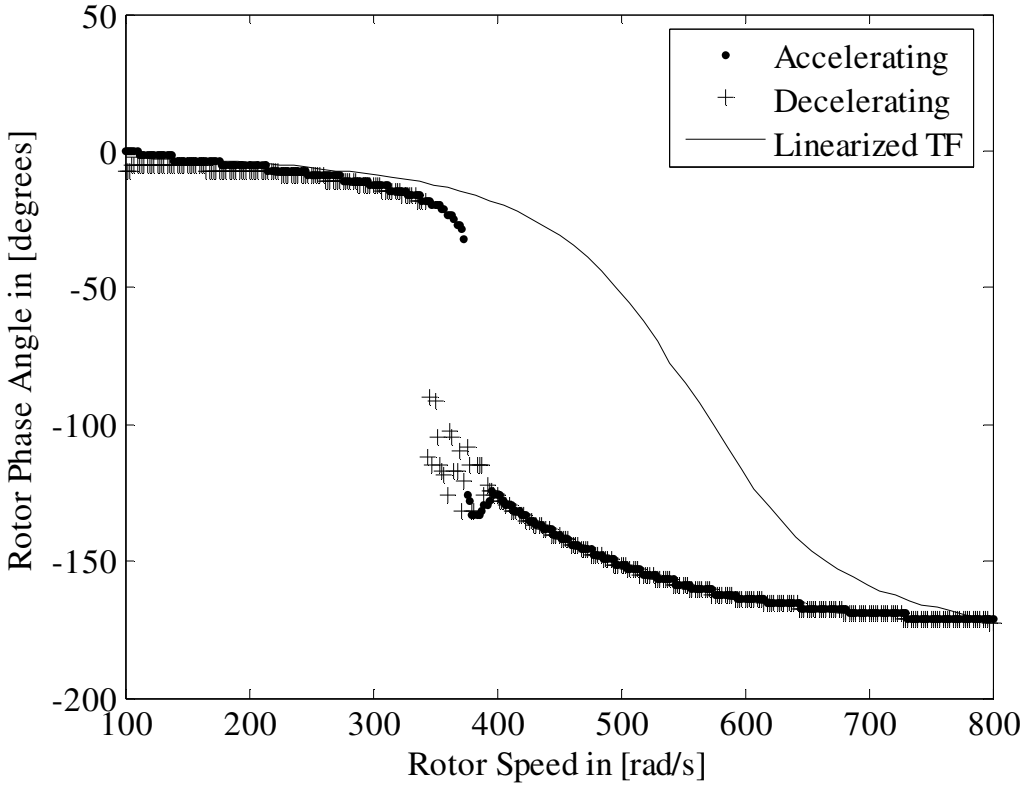

Figure 3.9 X-axis phase frequency response for softening spring behavior

At frequencies below the linear natural frequency, both linear and nonlinear system responses are in phase with the excitation input. Above the linear natural frequency, each system approaches a phase lag of -180° from the excitation input. This phase reversal causes the characteristic reduction in rotor oscillation amplitude at higher frequencies. For the softening spring proportional gains selected for this analysis, nonlinear phase reversal occurs at a lower frequency than the linearized system. The frequencies at which phase lag equals -90° closely match the jump frequencies for both increasing and decreasing rotor spin speeds.

3.4 SHOOTING METHOD

Since pole gap fluxes for the homopolar magnetic bearing must be computed by solving a set of linear magnetic circuit equations, analytical methods cannot be used to determine orbital equilibrium states and their stability. Fortunately, several numerical methods exist that do not require an analytical solution. Direct numerical integration can be carried out until stable steady state behavior is obtained. The stable frequency response curves shown in Figure 3.8 are generated using this direct method. However, direct numerical integration is unable to locate unstable orbital equilibrium states unless initial conditions lie exactly on an unstable orbit. Nonlinear magnetic bearing sensitivity to initial conditions makes it difficult to locate these unstable equilibrium states by arbitrary selection of initial conditions. A modified numerical integration routine known as the shooting method addresses this difficulty using an iterative algorithm to select initial conditions that lie exactly on orbital equilibrium paths regardless of their stability. Numerical integration from these initial conditions yields steady state rotor response without transient terms. This method is used to identify unstable orbits in the hysteresis region between amplitude jumps. The shooting method requires calculation of a numeric Jacobian that approaches the monodromy matrix when initial conditions lie on equilibrium paths. The eigenvalues of this monodromy matrix are called Floquet multipliers that can be used to determine local orbital equilibrium stability and classify bifurcation behavior. The iterative shooting algorithm is shown in Appendix A for reference.

The shooting method uses incremental initial state adjustments to step from an initial condition guess to an initial state resulting in steady state orbital equilibrium. With the shooting algorithm, orbital equilibrium states with an integer multiple, γ of the forcing period can be located within a specified error tolerance. For each iteration, the state adjustment η is computed from a numerically determined Jacobian J and the difference between the initial condition vector and the system state after γ forcing periods. This difference approaches zero along orbital equilibrium paths. The adjustment is calculated using

$$\eta = (J - I)^{-1}\left[x(0) - x(\gamma T_f)\right] \tag{39}$$

where I is the identity matrix. Convergence to orbital equilibrium requires modification of the state adjustment using a Newton-Raphson relaxation factor β. The value of β is decreased to locate highly unstable orbits and is increased to accelerate convergence to stable and moderately unstable orbital equilibrium paths. Convergence is considered achieved when the relative error falls below a defined error tolerance. This error represents the relative change for the next initial state guess and is determined by

$$e = \frac{\left\|x_{i+1}(0) - x_i(0)\right\|}{\left\|x_{i+1}(0)\right\|} \tag{40}$$

where the subscript indices represent the initial state for the current and next iterations. Shooting parameters used in this analysis and their values are shown in Table 3.4 for reference.

Table 3.4 Shooting algorithm parameters and values

Parameter	Symbol	Value
Periodicity of Response	γ	1
Relative Error Tolerance	e_{max}	10^{-6}
State Perturbation Magnitude	ε_j	10^{-9}
Relaxation Factor	β	0.2 to 0.5

To complete the amplitude frequency response curve in Figure 3.8, initial state guesses are determined by approximating the locus of unstable orbital amplitudes as a straight line between the data points before jumps in the stable frequency response curve. Since oscillation amplitudes recorded for stable frequency response analysis are phase-shifted from the periodic excitation force, these assumed initial conditions are modified so that they coincide with the beginning of a forcing period. This method allows computation of unstable synchronous orbital equilibrium paths by minimization of the relative error. It is assumed that unstable rotor orbits in the hysteresis region are synchronous with excitation frequency. In theory, initial conditions that lie exactly on an unstable equilibrium path will remain on the unstable orbit unless the system is

perturbed. In real simulations, truncation and roundoff errors can cause divergence from the desired orbit for highly unstable equilibrium paths. Local stability of orbital equilibrium states in non-autonomous nonlinear systems can be inferred from the stability of the linearized system near the equilibrium state. The shooting method is a useful tool for this nonlinear analysis because it yields multiple orbital equilibrium paths whose local stability can be determined using Floquet theory.

As the initial conditions approach an orbital equilibrium path, the numerically determined Jacobian approaches the monodromy matrix. With shooting, the Jacobian is formed one column at a time by integrating the governing equations for small perturbations, ε_j of each state from the assumed initial state. In Floquet theory, the monodromy matrix represents the nonlinear system solution with the identity matrix as the initial state vector. Eigenvalues of the monodromy matrix, known as Floquet multipliers are used to infer local stability of the nonlinear system. Since Floquet theory is based on a Taylor series expansion about the equilibrium state, it cannot be used to infer global stability. If the magnitudes of all Floquet multipliers are less than one, the orbital equilibrium state is a locally stable periodic attractor. If the magnitudes of all Floquet multipliers are greater than one, the equilibrium state is a locally unstable periodic repellor. When some eigenvalues have magnitude less than one and others have magnitude greater than one, the equilibrium state is classified as a saddle. The locus of unstable orbital equilibrium states that complete the amplitude frequency response curve have only one Floquet multiplier outside the unit circle and are therefore considered unstable saddles. The amplitudes of these unstable orbital equilibrium states are shown in Figure 3.10 for the hysteresis region near nonlinear resonance.

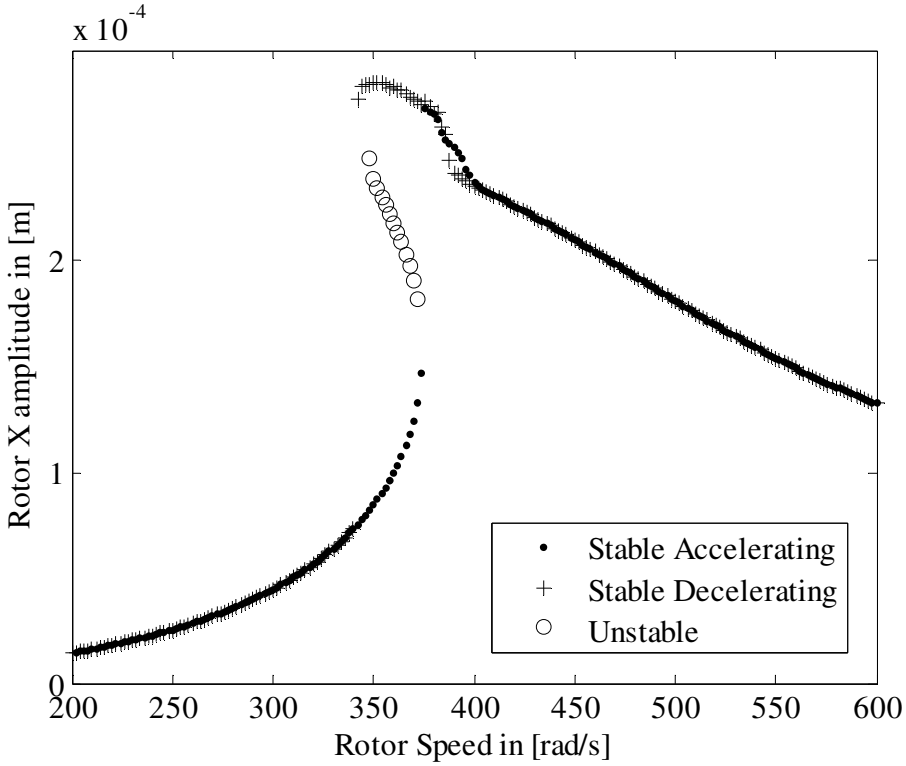

Figure 3.10 X-amplitude frequency response for stable and unstable equilibrium states

This locus of unstable orbital equilibrium states shows that the frequency response curve for softening-spring proportional control gains resembles the linearized model frequency response curve tilted to the left. While three orbital equilibrium states exist in the hysteresis region, only the center periodic orbit is unstable for all cases. Amplitude jumps between stable periodic orbits occur at vertical points of tangency of the composite frequency response curve. This behavior is analogous to frequency response of the well-known cubic Duffing oscillator. Extending this likeness to proportional control gains that result in nonlinear hardening spring behavior implies a resonant peak tilted to the right. As shown previously in Figure 3.7, nonlinear magnetic forces in hardening magnetic bearings do not deviate considerably from linear approximations so that the effect of this tilting would not be as significant as the softening magnetic bearing shown above.

As a system parameter such as rotor speed is varied, Floquet multipliers can migrate out of the unit circle along the positive real axis, along the negative real axis, or as complex conjugates. When these eigenvalues leave the unit circle the corresponding orbital equilibrium state transitions from locally stable to locally unstable periodic behavior. These changes in the local stability of an equilibrium state are known as bifurcations and the manner in which the Floquet multipliers exit the unit circle can be used to infer subsequent system behavior. This fact is exploited in Section 3.5 to classify bifurcations as cyclic-fold, period-doubling, or Neimark bifurcations.

3.5 BIFURCATION ANALYSIS

Nonlinearities in homopolar magnetic bearings result in rotor oscillations that may be attracted to one of several stable orbital equilibrium states. As shown by frequency response analysis, stable periodic rotor orbits may lose their stability or unstable orbits may become stable as a system parameter is varied. In addition, new frequency components may be introduced in stable periodic orbits that may or may not be commensurate with the original oscillation frequency. Such qualitative changes in nonlinear system response are called bifurcations. Different types of bifurcations are characterized by resulting dynamic behavior which can either evolve continuously from the original equilibrium state or may suddenly be attracted to another stable equilibrium state in a discontinuous manner [23]. This behavior is illustrated using iterated map functions such as bifurcation diagrams or Poincaré maps in which individual points represent instantaneous system states separated in time by multiples of the forcing period. Bifurcations can also be classified as described in Section 3.4 by the manner in which Floquet multipliers leave the unit circle. In the present bifurcation analysis, qualitative changes in nonlinear magnetic bearing response are explored using these tools for the region of the frequency response curve near nonlinear resonance where nonlinear effects are most apparent.

Two readily apparent bifurcation points in the nonlinear frequency response amplitude curve are the sudden amplitude jumps near 374 and 342 $^{rad}/_{s}$. These points

represent discontinuous bifurcations in which a locally stable orbital equilibrium state becomes unstable and the rotor is attracted to another stable orbit some distance away. Such bifurcations are called catastrophic or dangerous because oscillation amplitude may suddenly increase beyond allowable limits. The type of bifurcation responsible for these amplitude jumps is determined by the path of Floquet multipliers as rotor speed approaches the critical value. Real and imaginary parts of the Floquet multiplier that exits the unit circle are shown versus rotor speed in Figure 3.11a and on the complex plane in Figure 3.11b as rotor speed nears the upward jump bifurcation point.

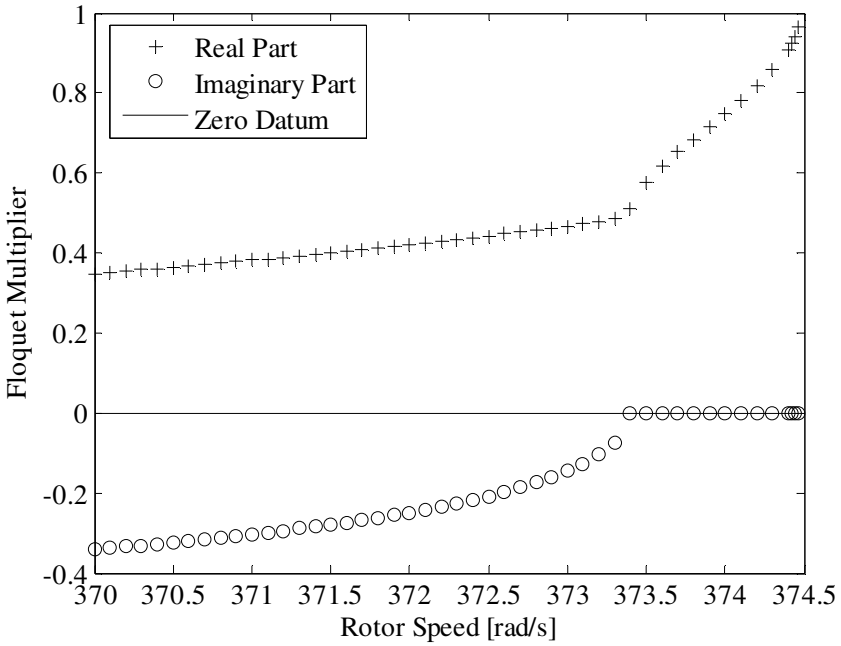

(a)

Figure 3.11 Migration of Floquet multiplier near upward jump bifurcation

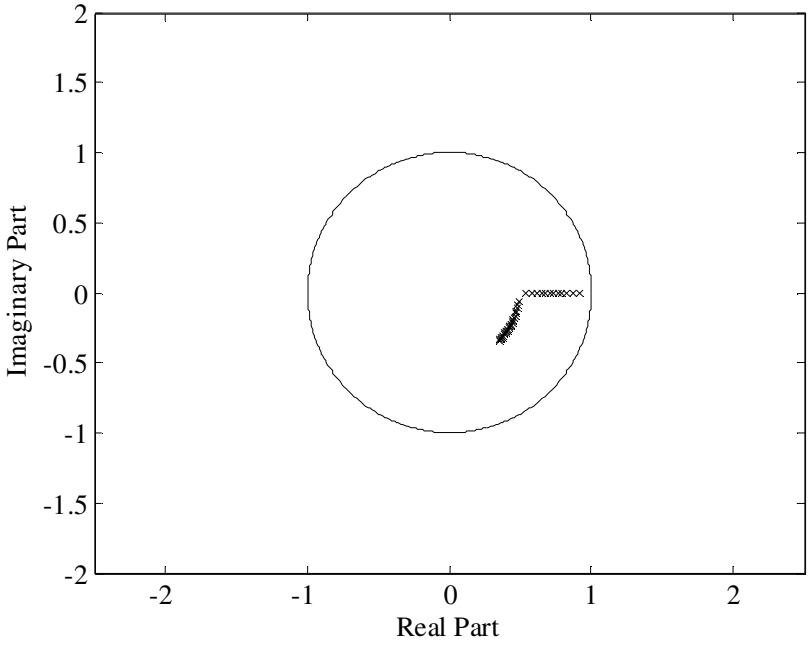

(b)

Figure 3.11 (continued)

As rotor speed is increased beyond the local stability limit, an eigenvalue of the monodromy matrix exits the unit circle along the positive real axis. This path indicates a saddle-node bifurcation such as transcritical, symmetry-breaking, or cyclic-fold [23]. Subsequent system behavior and corresponding vertical points of tangency in the bifurcation diagram reveal that this amplitude jump occurs by cyclic-fold bifurcation. Similar analysis of Floquet multipliers across the downward jump frequency is not feasible by numerical analysis because the period of stable rotor motion before the bifurcation is not an integer multiple of the forcing period.

Examination of the frequency response curves in Section 3.3 also reveals unpredictable rotor behavior in the frequency region near nonlinear resonance. These frequency response plots depict only one data point at each frequency corresponding to maximum rotor amplitude. However, this simplified portrayal is not complete for rotor orbits that are not periodic or contain asynchronous frequency components. To include these effects a bifurcation diagram is constructed by sampling the steady state rotor orbit

at multiples of the forcing period for different values of excitation frequency. Bifurcation diagrams show how equilibrium states respond as a control parameter such as rotor spin speed is varied. Each point in this bifurcation diagram represents instantaneous rotor position after an integer number of forcing periods for stable steady state oscillations. A bifurcation diagram is shown in Figure 3.12 for decreasing rotor spin speed to show the effect of sub-synchronous frequency components near resonance. Bifurcation behavior for increasing rotor spin speeds is not shown here because oscillations for the lower-amplitude orbital equilibrium states do not contain asynchronous frequency components. This linear behavior results from the close correlation between the linearized and non-linearized magnetic force for small rotor motions. For this reason, all subsequent bifurcation analysis only considers decelerating rotor spin speeds.

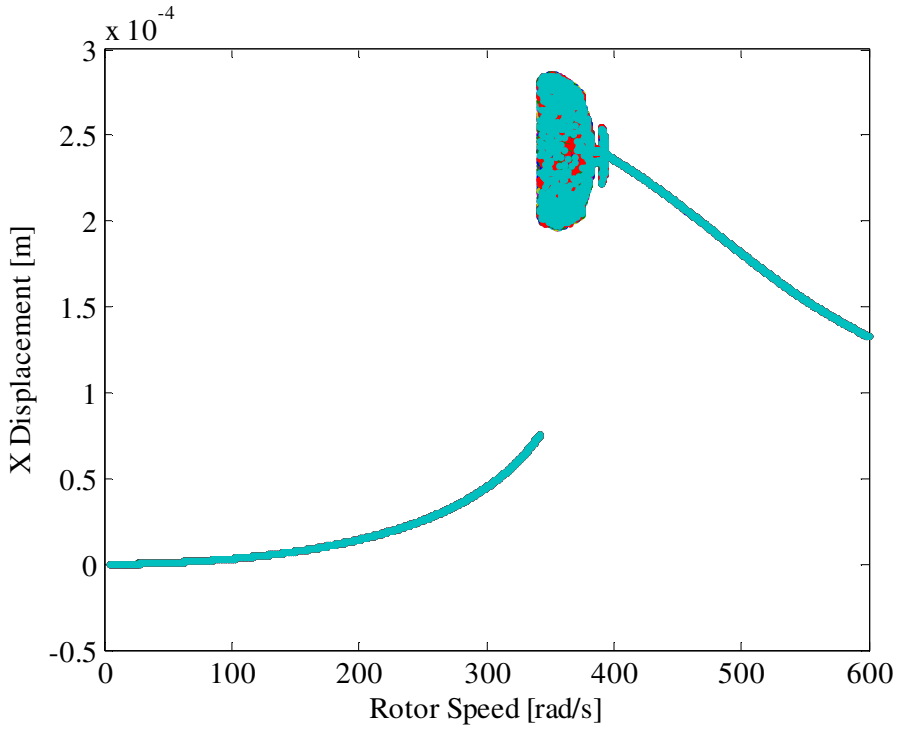

Figure 3.12 Bifurcation diagram for decreasing speed

Like linear systems, oscillations at rotor spin frequencies away from nonlinear resonance are synchronous with the excitation frequency. This is shown by the appearance of only one point at each frequency in the bifurcation diagram. As the rotor slows below $400\,{}^{rad}/_{s}$ the stable synchronous orbit begins to exhibit steady state response containing subharmonic frequency components. This could occur either by a secondary-Hopf (Neimark) bifurcation or through a series of period-doubling bifurcations at closely spaced frequency intervals. A closer view of the bifurcation diagram near nonlinear resonance is provided in Figure 3.13 where oscillations deviate from pure synchronous response.

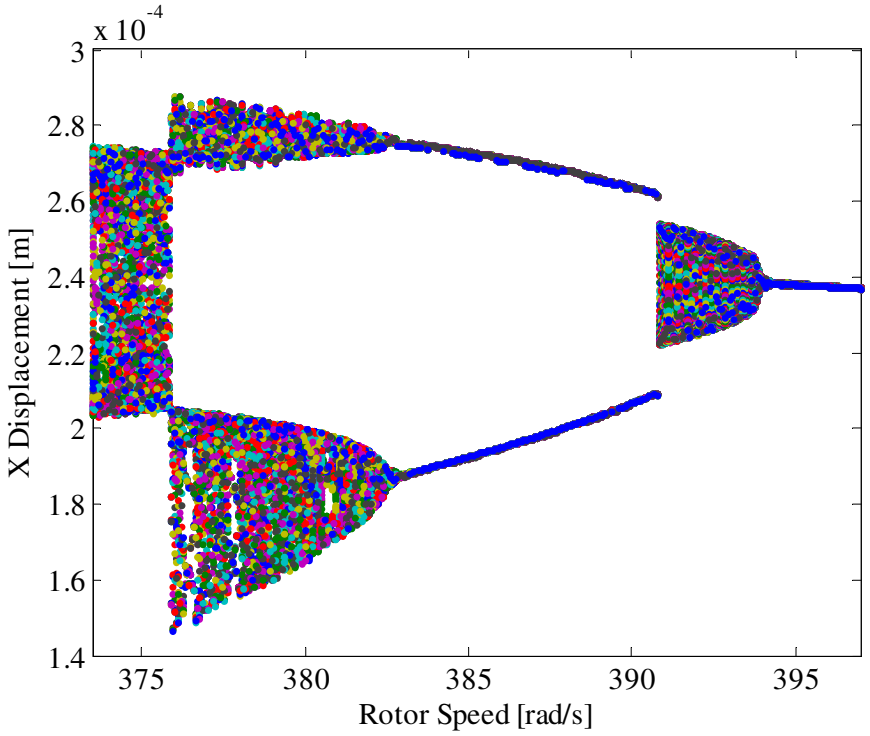

Figure 3.13 Bifurcation diagram for decreasing speeds near nonlinear resonance

The region near the first bifurcation point at ω=394 $\,{}^{rad}/_{s}$ is magnified in Figure 3.14 to show how incommensurate frequencies are suddenly introduced.

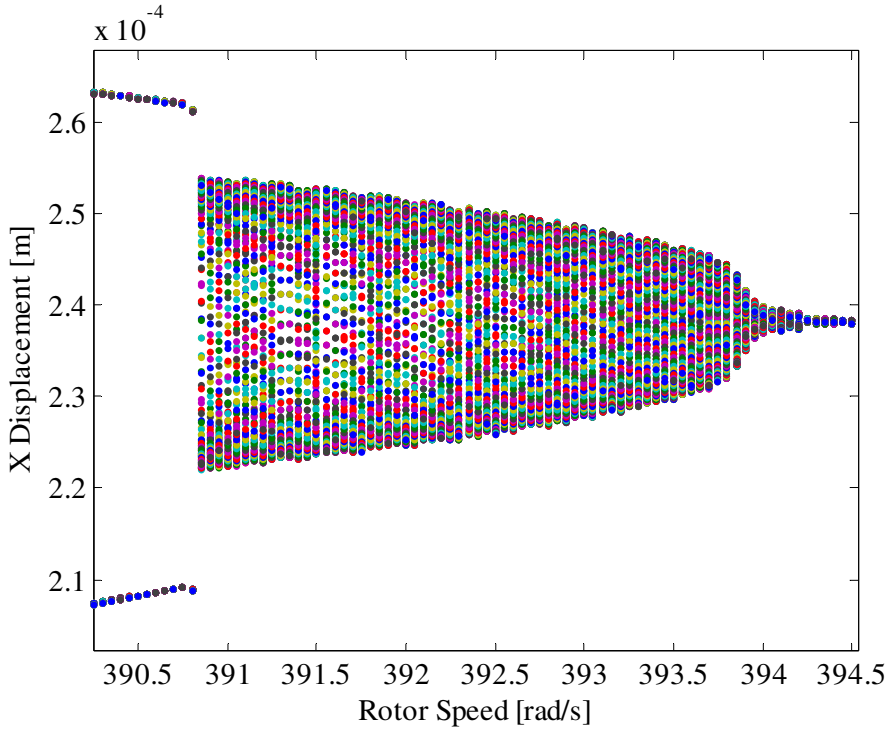

Figure 3.14 Bifurcation diagram for decreasing speeds near ω=394 $^{rad}/_{s}$

The particular bifurcations responsible for introducing these new frequency components are difficult to determine using the paths of Floquet multipliers since changes occur over such a small frequency range. Instead, periodicity of the resulting steady state response can be visualized using Poincaré maps. In contrast to bifurcation diagrams, this iterated mapping shows instantaneous rotor orbital position at multiples of the forcing period for just a single frequency. The Poincaré map in Figure 3.15 is used to identify steady state periodicity after the initial bifurcation by the number of visibly separate points. This map is constructed using one point for each of 300 forcing periods after transients have dissipated.

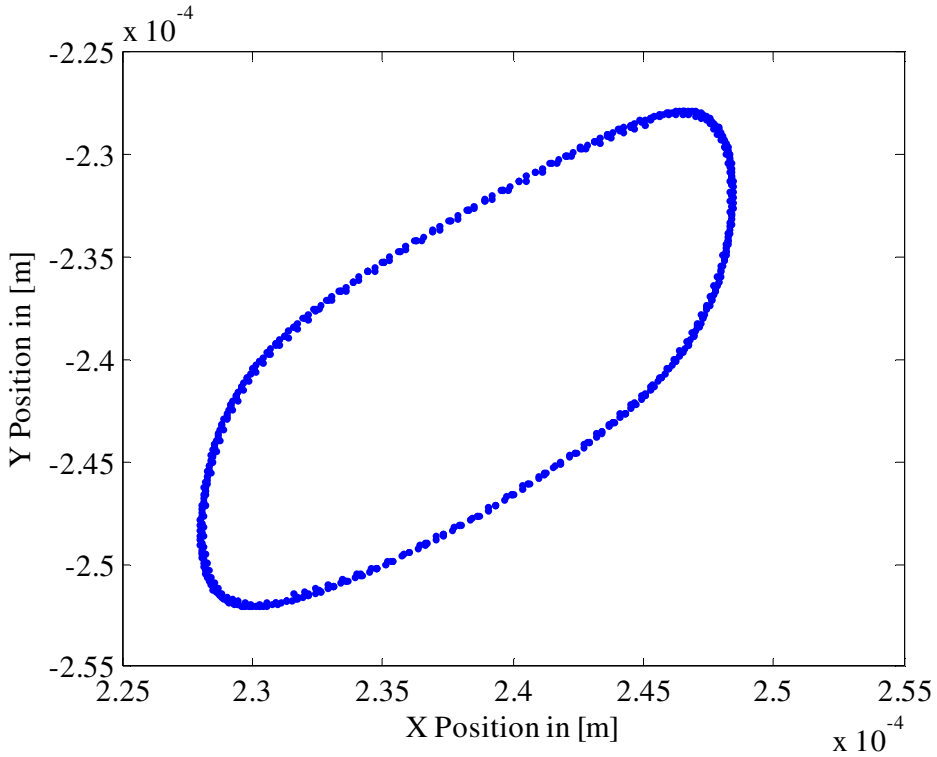

Figure 3.15 Poincaré map at ω=393 $^{rad}/_{s}$ showing quasiperiodic response

The closed curve in the Poincaré map consists of a large number of points at irregular intervals. This implies that incommensurate frequencies are introduced by a Neimark bifurcation. It is possible that period-doubling is also occurring simultaneously but the definite existence of non-integer subharmonic frequency components is evident from this mapping. Frequency content of the rotor vibration time signal for the X-direction is obtained by taking the 2^{19}-point DFT to ensure sufficient frequency resolution as shown in Figure 3.16. A hanning-type windowing function is applied to steady state response data to reduce leakage effects.

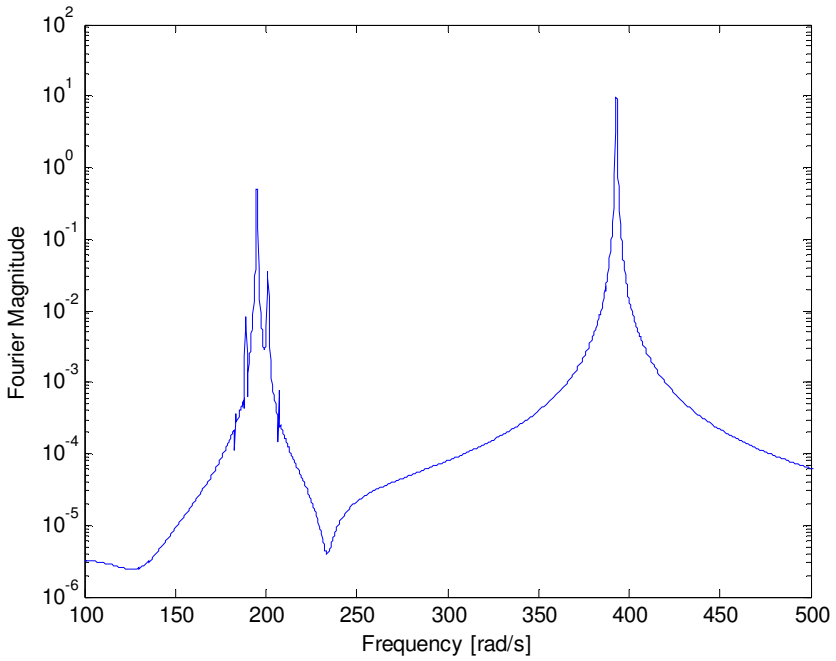

Figure 3.16 Frequency spectrum for quasiperiodic response at 392 $^{rad}/_{s}$

Analysis of this frequency spectrum reveals the existence a ½ subharmonic frequency component and several smaller sideband frequencies near this subharmonic which are incommensurate with the dominant frequency components. Nonzero amplitudes of the other frequencies near these spikes may be actually present but may also be due to residual leakage or truncation errors. The combined effect of these frequency components results in amplitude modulated, period-two steady state response as shown by the X-axis time signal in Figure 3.17 after transients have died out.

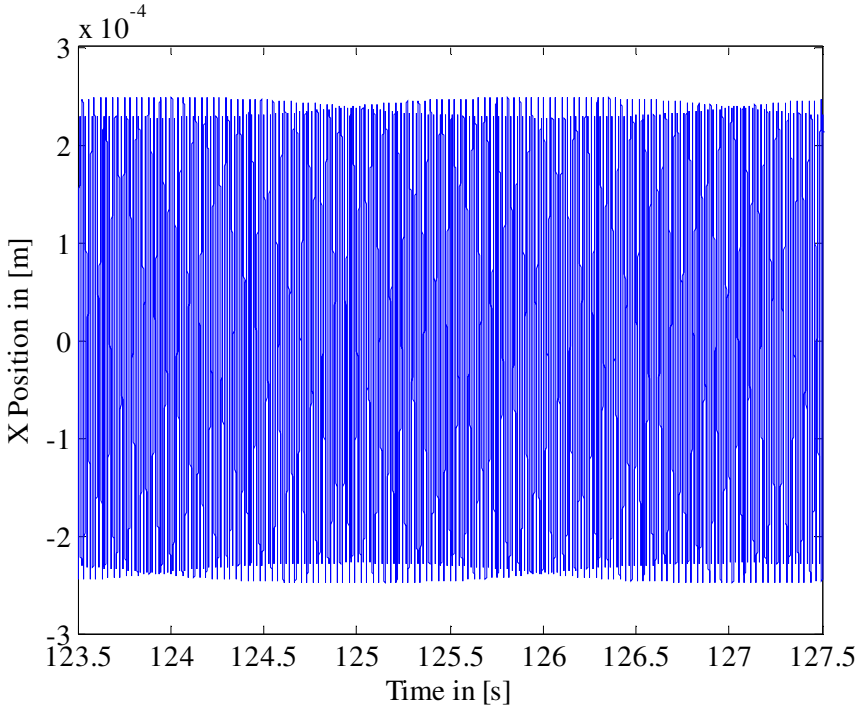

Figure 3.17 X-position time signal for quasiperiodic oscillations

As the rotor continues to slow, quasiperiodic oscillation amplitude increases uniformly until incommensurate frequency components suddenly disappear near 391 $^{rad}/_{s}$ in Figure 3.13. For a range of frequencies after this bifurcation between 391 and 383 $^{rad}/_{s}$ the rotor enters a stable period-two orbital equilibrium state with no amplitude modulation. For rotor speeds in this range only synchronous and ½ subharmonic frequency components remain. Rotor orbits for these frequencies consist of intersecting loops as shown in Figure 3.18.

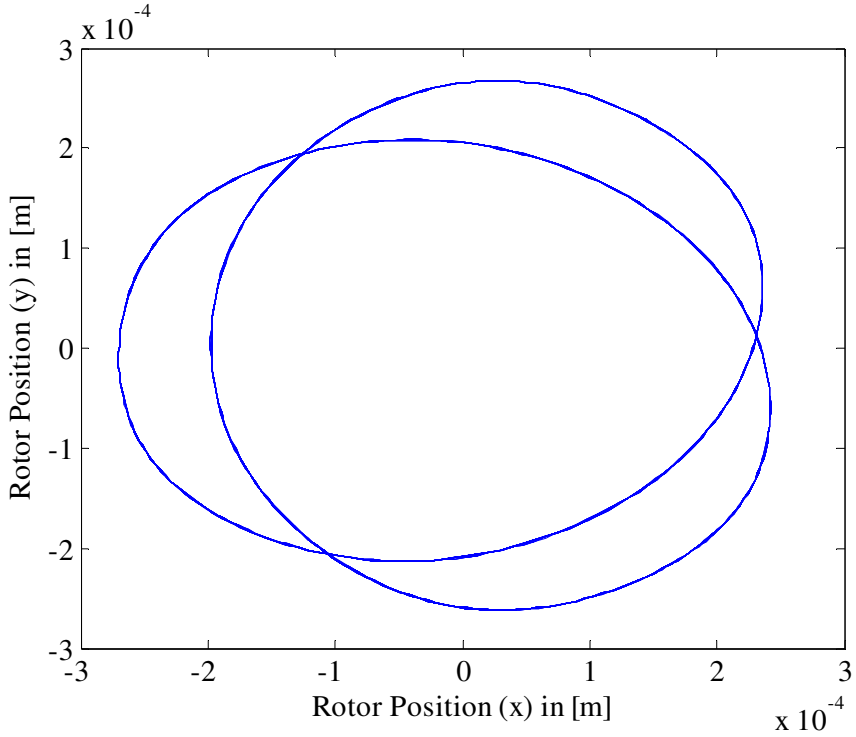

Figure 3.18 Rotor orbit for stable period-two equilibrium state at 387 $^{rad}/_{s}$

Continuing deceleration, these stable period-two orbits bifurcate again in a manner similar to the initial Neimark bifurcation at approximately 383 $^{rad}/_{s}$. Oscillation amplitudes continue to smoothly increase after incommensurate frequencies are reintroduced until the upward jump frequency near 374 $^{rad}/_{s}$ where a slight yet abrupt amplitude increase occurs. After this, rotor oscillations in the hysteresis frequency range contain incommensurate subharmonic frequencies with amplitudes that remain relatively constant until the downward amplitude jump.

3.6 SUMMARY

This analysis reveals several differences between nonlinear rotor response and linearized model predictions for homopolar magnetic bearings. Governing equations are developed for both linear and nonlinear magnetic force terms using magnetic circuit equations and bias linearization. Bearing stiffness for each system is related to proportional control gain to define values that result in hardening spring, softening spring and unstable behavior. This shows that nonlinear magnetic force is closely approximated by the linear model for rotor deflections up to almost half the bearing clearance. Softening spring proportional control gains are selected to magnify nonlinearities for frequency response analysis.

Bifurcation behavior of the homopolar magnetic bearing is studied using numerical methods to generate frequency response curves and bifurcation diagrams. These plots show behavior similar to the cubic softening Duffing oscillator such as tilting of the resonant peak to lower excitation frequencies and amplitude jumps resulting in multiple stable orbital equilibrium states. Amplitude jumps are shown to occur by cyclic-fold bifurcations using the paths of Floquet multipliers and vertical points of tangency of the composite frequency response curve. At frequencies near nonlinear resonance during rotor deceleration, rotor oscillations experience period-doubling and Neimark bifurcations resulting in subharmonic frequency content. This analysis can be used to operate homopolar magnetic bearings at higher spin speeds or to support larger, more imbalanced rotors with increased knowledge of excitation frequency effects on nonlinear rotor oscillations.

CHAPTER IV

CONCLUSIONS

4.1 CIRCULAR SENSOR ARRAY

The circular sensor can effectively remove certain harmonics of runout from the rotor position signal when all sensors in the array are operational. This is achieved by weighting individual eddy-current probe voltages using a weighting gain matrix (WGM) to produce two independent array output signals. Runout reduction performance of the unfailed sensor array is shown using analytical expressions for the magnitude of individual harmonics, by numerical simulations on a sample runout pattern, and by actual testing on a prototype 8-sensor array. The ideal n-sensor array with no sensor failures successfully removes signal harmonics $k = 2$ to $k = n$-2 to deliver an improved position measurement to the AMB controller with reduced runout error. The prototype sensor array significantly reduces these runout harmonics but does not achieve complete elimination due to electronic component imperfections in the drive circuit.

Two approaches are available for mapping individual sensor voltages to array outputs in the presence of sensor failures. The swap-in-approach (SIA) replaces the WGM to account for the particular sensors lost, requiring additional fault-detection hardware and increased memory space. The no-swap-in approach (NSIA) maintains the unfailed WGM for all failure states but results in incomplete runout reduction and synchronous measurement error after individual sensor failures. The NSIA is employed for this analysis and runout and measurement error are evaluated for selected failure configurations. Single sensor failures of on-axis and off-axis sensors are investigated by numerical simulations using an 8-sensor and a 16-sensor array. Single failure of sensors that are located on a measurement axis are shown to increase runout and measurement error in only one array output as predicted using analytical expressions. Single failure of sensors that are not located directly on a measurement axis are shown to increase runout and measurement error in each array output. The effect of single sensor failures can be accurately predicted using (9) for the ideal sensor array. If the location of the failed

sensor is known, synchronous measurement error can be corrected for single failures using the amplitude adjustment factors in (11). Failure of opposing sensor pairs is also investigated by numerical simulations of an 8-sensor and a 16-sensor array. In these failure configurations, even harmonics of runout are eliminated while the magnitudes of odd harmonics depend on failed sensor pair location. While odd harmonic amplitudes for sensor pair failures follow similar trends as single sensor failures, analytical expressions to predict these amplitudes are not as accurate. For the failure configurations studied here, loss of an opposing pair of on-axis sensors has the greatest effect on sensor array output signals. In this worst-case scenario, the ratio of runout harmonics present in the failed array to those in the unfailed array is 0.500 and synchronous amplitude detected by the failed array is exactly ½ the amplitude of actual target motion.

The prototype drive circuit used to operate individual sensors and implement the WGM is constructed using variable components to optimize sensor array sensitivity and linearity during the design stage. Variations in individual capacitances and resistances due to this flexibility result in incomplete runout reduction and slight differences in sensitivity for each measurement axis. Despite these imperfections, linearity and sensitivity are comparable to commercial eddy-current position measurement systems. The drive circuit is also designed to reduce sources of measurement noise. Sensor crosstalk is avoided by driving all eddy-current probes using a common carrier signal. Thermal drift and common-mode noise radiated into the cables is reduced by driving opposing probes differentially due to anti-symmetry in the unfailed WGM. This design results in less measurement noise than commercial systems but precludes sensor array operation in the presence of sensor failures. Design revisions are suggested to allow fault-tolerance in future circuit models as intended. These revisions require separate amplification and demodulation of individual probe voltages and use of stable electronic components for symmetric sensitivity and improved runout reduction. Rotational testing of the prototype 8-sensor array reveals significant reduction of runout harmonics present in the test rotor. While the prototype sensor array does not perform as well as idealized

simulations, synchronous vibration components in sensor array output signals are much more apparent than in single sensor measurements. These improvements in the rotor position measurement system translate into more efficient control of synchronous vibrations and reduced heating of power amplifiers in the AMB control system.

4.2 NONLINEAR ANALYSIS OF HOMOPOLAR MAGNETIC BEARINGS

Nonlinearities in homopolar magnetic bearings are studied using numerical methods to identify orbital equilibrium states and their behavior as excitation frequency is varied. Governing equations for rotor motions in a simplified radial homopolar magnetic bearing are derived from magnetic circuit equations. Bias linearization is used to determine position and voltage stiffness terms from the nonlinear model. Using PD feedback control, a minimum value of proportional control gain exists above which the magnetic bearing provides a stabilizing stiffness force. This minimum control gain is equivalent for the nonlinear and linearized magnetic bearing models. Nonlinear magnetic stiffness is closely approximated by the linear model for small rotor deflections. As rotor position nears the bearing clearance, nonlinear magnetic force deviates from the linear model in a manner influenced by the value of proportional control gain. The homopolar magnetic bearing behaves as a hardening spring for intermediate values and as a softening spring for higher values of proportional control gain. While hardening spring behavior is desirable, proportional gains that result in softening spring behavior must be selected for high speeds and large or highly imbalanced rotors due to maximum force limitations. For the values of proportional control gain used in this analysis, nonlinear effects become significant when the ratio of rotor oscillation amplitudes to bearing clearance approaches 0.47.

Frequency response curves for the nonlinear magnetic force term are generated by direct numerical integration and are compared to linear model predictions. Rotor oscillation amplitude and phase closely match the linear model for frequencies well below and above the linearized natural frequency but differ in their behavior near resonance. Maximum rotor amplitude for proportional control gains that result in

nonlinear softening spring characteristics occurs at a lower frequency than the linearized model prediction. The amplitude frequency response curve appears tilted to the left and includes a hysteresis region in which three orbital equilibrium states exist at the same frequency. Local stability of the upper and lower equilibrium orbits depends on the direction of rotor angular acceleration while the middle equilibrium orbit is unstable for all cases and cannot be determined by direct numerical integration alone. The locus of unstable orbital equilibrium states in the hysteresis region of the frequency response curve is determined using the shooting method with assumed initial conditions. The composite frequency response curve for the homopolar magnetic bearing resembles behavior of the cubic Duffing oscillator. At vertical points of tangency in the composite amplitude curve, a locally stable orbital equilibrium state becomes unstable through a cyclic-fold bifurcation and the response is attracted to the other stable orbit. Nonlinear system phase lag curves also include a region of hysteresis where steady state response is different for increasing and decreasing rotor speeds. Phase angles at the jump frequencies are approximately -90° for both locally stable orbital equilibrium states.

Several frequency-dependent bifurcations occur at frequencies near nonlinear resonance. Amplitude jumps observed in frequency response curves are caused by cyclic-fold bifurcations as shown by the migration of numerically determined Floquet multipliers along the positive real axis. While the lower-amplitude orbital equilibrium state consists of pure synchronous response, the higher-amplitude orbit contains incommensurate frequency components resulting in quasiperiodic response. This difference in stable orbital equilibrium behavior is attributed to the divergence of nonlinear magnetic stiffness from the linearized stiffness for larger rotor deflections. Quasiperiodic motion is thought to be caused by simultaneous period-doubling and Neimark bifurcations. Frequency content of the amplitude modulated rotor orbit reveals a ½ subharmonic and multiple sideband frequency components. For a narrow range of frequencies, incommensurate frequency components disappear and only the synchronous and ½ subharmonic remain. This stable period-two motion increases in amplitude until it experiences another simultaneous period-doubling and Neimark bifurcation in which

incommensurate frequencies appear again and persist until the downward amplitude jump where stable synchronous motion resumes. For the magnetic bearing model studied here, the most significant nonlinear effects are quasiperiodic motion and sudden amplitude jumps that occur at predictable frequencies if model parameters are known. While chaotic rotor oscillations are not observed in this model, consideration of flux saturation may reveal different results.

Nonlinear rotor oscillations in homopolar magnetic bearings can be avoided by minimizing rotor mass and eccentricity and by operation at low spin speeds. For these conditions the nonlinear magnetic force is very nearly linear with respect to rotor position. The critical amplitude for which nonlinear magnetic force effects become more pronounced in rotor response is influenced by bearing clearance and by proportional control gain. Simulations such as those used in this analysis can be used to determine safe operating speeds for existing rotor-bearing systems or to aid in the design of new magnetic bearings for specified operating conditions.

4.3 FUTURE WORK

While the circular sensor array and analysis of nonlinearities in homopolar magnetic bearings presented here provide many opportunities to improve magnetic bearing performance, this work may be continued by the interested researcher. Fault tolerance of the circular sensor array is evaluated here using simulations of an ideally constructed array, but the prototype system tested does not allow individual sensor failures. Design modifications to the prototype drive circuit are provided in Section 2.7 to allow this capability and to improve measurement accuracy and runout reduction. Additionally, the possibility of using a 12-sensor array may be worth pursuing to increase the number of runout harmonics eliminated and decrease the effect of single sensor failures. To allow fault tolerance to single sensor failures using the NSIA, implementation of the amplitude adjustment factors should also be investigated.

To further understand nonlinear effects in homopolar magnetic bearings, an analytical approach is best. The author does not currently possess the mathematical

skills to perform conventional nonlinear analysis of second-order differential equations with embedded systems of coupled equations. If these equations could be nondimensionalized and decoupled, the results obtained here could be generalized for an arbitrary homopolar magnetic bearing using harmonic balance, trigonometric collocation, Floquet theory, or the method of multiple scales. Numerical analysis performed in this work could also be extended to investigate the effects of gravity, rotor mass, unbalance eccentricity, flux saturation or flexible rotor models. This would require modification of the governing equations but makes results more applicable to real world scenarios.

Whether by the suggested continuation of this work or through alternate means, research will doubtless continue to extend the performance limits of magnetic bearings. These electromechanical devices transcend conventional constraints of mechanical roller supports through minimal friction, zero wear and the ability to control rotor motions and transmitted vibration forces. While magnetic bearings create unique problems in their design and implementation, they offer unique opportunities for the future.

REFERENCES

[1] C.R. KNOSPE 1991 *Proceedings of the International Symposium on Magnetic Suspension Technology*, Hampton, Virginia, USA, 181. Stability and performance of notch filters for unbalance response.

[2] R. HERZOG, P. BUHLER, C. GAHLER and R. LARSONNEUR 1996 *IEEE Transactions on Control Systems Technology* **4**, 580-586. Unbalance compensation using generalized notch filters in multivariable feedback of magnetic bearings.

[3] BENTLY NEVADA CORPORATION 1979 *Application Note L0196*, Minden, NY. Vector nulling versus runout compensation.

[4] C.-S. KIM and C.-W. LEE 1997 *IEEE/ASME Transactions on Mechatronics* **2**, 51-57. In situ runout identification in active magnetic bearing system by extended influence coefficient method.

[5] J.D. SETIAWAN, R. MUKHERJEE, E. H. MASLEN, and G. SONG 1999 *Proceedings of IEEE/ASME International Conference on Advanced Intelligent Mechatronics*, Atlanta, Georgia, USA, 800-805. Adaptive compensation of sensor runout and mass unbalance in magnetic bearing systems.

[6] J.D. SETIAWAN, R. MUKHERJEE and E. H. MASLEN 2001 *ASME Journal of Dynamic Systems, Measurement, and Control* **123**, 211-218. Adaptive compensation of sensor runout for magnetic bearings with uncertain parameters: theory and experiments.

[7] J.D. SETIAWAN, R. MUKHERJEE and E. H. MASLEN 2002 *Journal of Dynamic Systems, Measurement, and Control* **124**, 14-24. Synchronous sensor runout and unbalance compensation in active magnetic bearings using bias current excitation.

[8] P.D. CHAPMAN 1985 *Journal of Precision Engineering* **7**, 129-137. A capacitive based ultraprecision spindle error analyser.

[9] H.-J. AHN and D.-C. HAN 2003 *Measurement Science and Technology* **14**, 531-542. Optimal multi-segment cylindrical capacitive sensor.

[10] M.-H. LI 2004 *Ph.D. Dissertation, Texas A&M University*, Fault tolerant control of homopolar magnetic bearings and circular sensor arrays.

[11] E.H. MASLEN, P.E. ALLAIRE, M.D. NOH and C.K. SORTORE 1996 *Journal of Tribology* **118**, 839-846. Magnetic bearing design for reduced power consumption.

[12] M. CHINTA 1997 *Ph.D. Dissertation, Texas A&M University*, Steady state nonlinear rotordynamics and modeling of magnetic bearings.

[13] M. CHINTA and A.B. PALAZZOLO 1998 *Journal of Sound and Vibration* **214**(5), 793-803. Stability and bifurcation of rotor motion in a magnetic bearing.

[14] J.C. JI and C.H. HANSEN 2001 *Journal of Sound and Vibration* **240**(4), 599-612 Nonlinear oscillations of a rotor in active magnetic bearings.

[15] M.E.F. KASARDA, P.E. ALLAIRE and P.M. NORRIS 1999 *Journal of Engineering for Gas Turbines and Power* **121**(4), 697-702. Experimentally determined rotor power losses in homopolar and heteropolar magnetic bearings.

[16] C. KIM 1995 *Ph.D. Dissertation, Texas A&M University*, Magnetic bearing eddy current effects on rotordynamic system response.

[17] U.J. NA 2004 *Journal of Sound and Vibration* **272**, 495-511. Fault tolerance of homopolar magnetic bearings.

[18] A. KENNY 2001 *Ph.D. Dissertation, Texas A&M University*, Nonlinear electromagnetic effects on magnetic bearing performance and power loss.

[19] BENTLY NEVADA CORPORATION 2005 *http://www.bently.com* 3300 XL 8 mm proximity transducer system, specifications and ordering information, revision G.

[20] S.D. ROACH 1998 *Sensors* **15**(9), 56-74. Designing and building an eddy current position sensor.

[21] R.H. JANSEN, R. LEBRON, T.P. DEVER and A.G. BIRCHENOUGH 2003 *Proceeding of the 1st International Energy Conversion Engineering Conference*, Portsmouth, Virginia, USA, AIAA-2003-6107. PWM switching frequency effects on eddy current sensors for magnetically suspended flywheel systems.

[22] T.P. DEVER, A. B. PALAZZOLO, E.M. THOMAS III and R.H. JANSEN 2001 *Proceedings of the 36th Intersociety Energy Conversion Engineering Conference*, Savannah, Georgia, USA, 689-694. Evaluation and improvement of eddy current position sensors in magnetically suspended flywheel systems.

[23] A.H. NAYFEH and B. BALACHANDRAN 1995 *Applied Nonlinear Dynamics*. New York: John Wiley and Sons.

APPENDIX A SHOOTING ALGORITHM

1. Define magnetic bearing parameters
    a. Mass properties (m, e, c, A_{pole}, A_{PM})
    b. Magnetic properties (N, H, B_{sat}, F_F, F_L, μ_0, μ_{PM})
    c. Controller parameters (G_p, G_d, CDM)
    d. Operating parameters (ω, T_f)
2. Define shooting variables (e_{max}, ε_j, γ, α)
3. Initialize shooting parameters (error, r_{max}, v_{max})
4. For n different initial condition guesses
    a. Generate random initial state guess $x_{guess,i}$
        i. Check that $|x_{guess,i}| < r_{max}$
        ii. Check that $|v_{guess,i}| < v_{max}$
    b. While error < e_{max}
        i. Integrate governing equations from 0 to γT_f using initial guess
        ii. Extract final state values $x_i(\gamma T_f)$
        iii. For each state k
            1. Perturb initial conditions by ε_j
            2. Integrate governing equations from 0 to γT_f using perturbed initial conditions
            3. Extract final values $x_e(\gamma T_f)$
            4. Form the k^{th} column of the Jacobian

$$J(k) = \frac{\left[x_i(\gamma T_f) - x_e(\gamma T_f)\right]}{\varepsilon_j}$$

        iv. Assemble Jacobian
        v. Adjust nth guess by η using relaxation factor α

$$\eta = \left(J - I\right)^{-1}\left[x(0) - x(\gamma T_f)\right]$$

        vi. Calculate new error in x_{guess}

$$error = \frac{\left\| x_{guess,i+1} - x_{guess,i} \right\|}{\left\| x_{guess,i+1} \right\|}$$

VITA

Robert “Kyle” Wiesenborn received his Bachelor of Science degree in mechanical engineering from Texas A&M University in 2004. He entered the graduate program the following semester and worked as a teaching assistant for various courses while pursuing a graduate degree. In 2006 he received his Master of Science degree in mechanical engineering from Texas A&M University and began working at Schlumberger in Sugar Land, TX.

Kyle may be reached at 16802 Pheasant Creek Court, Sugar Land, TX 77478 or by email at kwiesenborn@gmail.com.